MATERIALS SCIENCE

Swarming magnetic nanorobots bio-interfaced by heparinoid-polymer brushes for in vivo safe synergistic thrombolysis

Manyi Yang[1]†, Yaoyu Zhang[2,3]†, Fangzhi Mou[1]*, Chuan Cao[1], Lingxia Yu[1], Zhi Li[3]*, Jianguo Guan[1,4]*

Biocompatible swarming magnetic nanorobots that work in blood vessels for safe and efficient targeted thrombolytic therapy in vivo are demonstrated. This is achieved by using magnetic beads elaborately grafted with heparinoid-polymer brushes (HPBs) upon the application of an alternating magnetic field B(*t*). Because of the dense surface charges bestowed by HPBs, the swarming nanorobots demonstrate reversible agglomeration-free reconfigurations, low hemolysis, anti-bioadhesion, and self-anticoagulation in high-ionic-strength blood environments. They are confirmed in vitro and in vivo to perform synergistic thrombolysis efficiently by "motile-targeting" drug delivery and mechanical destruction. Moreover, upon the completion of thrombolysis and removal of B(*t*), the nanorobots disassemble into dispersed particles in blood, allowing them to safely participate in circulation and be phagocytized by immune cells without apparent organ damage or inflammatory lesion. This work provides a rational multifaceted HPB biointerfacing design strategy for biomedical nanorobots and a general motile platform to deliver drugs for targeted therapies.

INTRODUCTION

Micro-/nanorobots (MNRs) can convert environmental energy into their own kinetic energy. Similar to living organisms in nature, they may further exhibit emerging collective behaviors, such as enhanced propulsion and intelligent responsiveness to local environments, by gathering into coherent groups purely through local interactions (*1*–*5*). With powerful propulsions, MNRs are promising for precisely delivering (or retrieving) cargoes to (or from) hard-to-reach organs or tissues and thus may bring about revolutionary changes to biomedical research and clinical practice, such as targeted drug/gene/cell delivery, detoxification, and microsurgery (*6*–*12*).

To realize biomedical applications, MNRs are frequently designed using biocompatible materials, endogenous fuels, and/or external-field powering strategies (*13*–*17*). For instance, by harnessing the biofriendly nature of the chemical reactions between metal magnesium and biofluids (*18*), Mg-based micromotors can effectively work in gastric media and deliver antibiotic drugs to treat stomach infections (*19*, *20*). Urease-powered nanomotors using endogenous urea as fuels can work in blood circulation system (*21*) and exhibit active homogeneous distribution and enhanced fluid mixing for bladder tumor targeting and drug delivery upon intravesical injection into a bladder (*22*). Bioinspired hybrid microrobots by natural microalgae can improve cargo delivery in gastrointestinal tissue and active delivery of antibiotics in the lungs in vivo (*23*, *24*). Using biocompatible fuel-free magnetic propulsions, magnetic microrobots are demonstrated to actively deliver drugs to malignant glioma and perform ulcer healing in vivo, respectively (*25*, *26*).

Moreover, the interface engineering of MNRs with biological systems plays important roles in their self-propulsion, colloidal stability, opsonization, and biological performance (*27*). Chemically powered microswimmers, after being coated with polyelectrolyte, can avoid the quenching of self-propulsion in biofluids (*28*). Magnetic micropropellers or microswarms modified with liquid perfluorocarbon coating are capable of operating in the dense vitreous body of the eye or biofluids because of the greatly reduced interaction with biopolymers and minimized viscous drag (*2*, *29*). Cloaking MNRs with cell membranes may avoid nonspecific opsonization and immune clearance and enhance their blood circulation time and targeting efficiency (*30*).

Motivated by the continuous advancement of MNRs and the serious, even life-threatening cardiovascular diseases caused by thrombosis, researchers have devoted considerable attention to exploring the utilization of MNRs as a promising and efficient therapeutic approach for the effective treatment of thrombosis (*8*, *9*, *31*–*38*). For instance, in vitro and in vivo experiments have demonstrated that light-driven micro/nanomotors cloaked by platelet or erythrocyte membranes can execute thrombolytic treatment by self-targeting the thrombus site, delivering thrombolytic drugs in a controllable sequential mode and/or deeply penetrating in thrombus site under near-infrared irradiation (*8*, *33*). Recently, chemotactic neutrophils equipped with a urease motor have also been demonstrated to be capable of targeting a thrombus and promoting thrombolysis by delivering thrombolytic protein drugs of urokinase there (*34*). Despite the improved bioavailability and biosafety of thrombolytic drugs with greatly reduced hemorrhagic side effects, they suffer from weak propulsion, especially during the targeting process, and primarily function as single robots in thrombolysis. These features make their accumulation time at thrombus long, thus hindering the time-critical thrombolysis therapy. Alternatively,

[1]State Key Laboratory of Advanced Technology for Materials Synthesis and Processing, International School of Materials Science and Engineering, Wuhan University of Technology, Wuhan 430070, P. R. China. [2]School of Medicine, Wuhan University of Science and Technology, Wuhan 430081, P. R. China. [3]Department of Orthopedics, General Hospital of Chinese PLA Central Theater Command, Wuhan 430070, P. R. China. [4]Wuhan Institute of Photochemistry and Technology, 7 North Bingang Road, Wuhan 430083, P. R. China.
*Corresponding author. Email: moufz@whut.edu.cn (F.M.); lizhi301@163.com (Z.L.); guanjg@whut.edu.cn (J.G.)
†These authors contributed equally to this work.

magnetic MNRs show powerful locomotion, precise navigation, and emerging collective behaviors, exhibiting great potential in fast thrombolysis. They can perform thrombolysis by mechanically disturbing local fluids to enhance the diffusion or mass transportation of free thrombolytic drugs (*35*–*38*) or by delivering the loaded thrombolytic drugs to occlusive blood clots in blood vessels under external magnetic field navigation (*31*, *32*, *39*). However, the magnetic nanoparticles (NPs) serving as the building blocks of the so far developed magnetic MNRs face a great challenge of suppressed interparticle repulsion when exposed to high-ionic-strength media, potentially leading to severe aggregation and bioadhesion in blood vessels (*40*, *41*). This limitation exposes their clinical thrombolysis applications to significant risks and serious side effects, such as off-target toxicity, blood capillary clogging, and exogenously stimulated thrombosis (*42*, *43*).

Here, we demonstrate that swarming magnetic nanorobots bio-interfaced by heparinoid-polymer brushes (HPB-NRs) can work in blood vessels and accomplish targeted thrombolytic therapy safely and efficiently in vivo. In this protocol, NPs of magnetic beads elaborately grafted with heparinoid polystyrene sulfonate sodium brushes (MB@PSS NPs) are prepared by surface-initiated atom transfer radical polymerization (ATRP). The heparinoid-PSS brushes enable them to show excellent dispersity in blood as individual particles because of their enhanced surface charge density in high-electrolyte media, while they are assembled into biocompatible swarming HPB-NRs with strong thrusts and precise navigation under $\mathbf{B}(t)$. The as-constructed swarming HPB-NRs hold strong anticoagulation, low hemolysis, anti-agglomeration, and anti-bioadhesion in whole blood environments. After being loaded with massive drugs, they can further achieve synergistic thrombolysis in vitro and in vivo by motile-targeting drug delivery and mechanical destruction. Moreover, upon the completion of thrombolysis and removal of $\mathbf{B}(t)$, the HPB-NRs automatically disassemble into individual particles dispersed in blood and are allowed to be phagocytized by immune cells with no obvious organ damage or inflammatory lesion, indicating its high biosafety. This work provides a rational interface design strategy for nanorobots working in blood flow and offers an insight into them. Compared to previous magnetic NPs or MNRs for thrombolysis, the HPB-NRs developed here have a critical advantage of reversible switch between collective states (swarming nanorobots) and dispersed states (dispersing NPs) in blood environments in response to $\mathbf{B}(t)$, besides the efficient thrombolysis. The developed nanorobots are expected to act as a general motile platform to deliver drugs for targeted therapies.

RESULTS

Conceptual design

For nanorobots working in blood vessels (sometimes called injectable nanorobots), they should be compatible with the blood environment, including high blood dispersity, good anticoagulation, and negligible hemolysis (*7*). Heparinoid substances contain large quantity of functional $-SO_3^-$ or $-COO^-$ groups that can gain dense surface charges and bind with antithrombin III (AT III). They exhibit excellent anticoagulation in blood and stop the blood clotting cascade (*44*). Thus, MB@PSS NPs (Fig. 1, A and B) are fabricated by surface-initiated ATRP and designed as the building blocks of swarming magnetic nanorobots, named as swarming HPB-NRs. With the surface heparinoid-PSS brushes, the MB@PSS NPs gain dense surface charges, which enable them to be well-dispersed as individual building blocks in high-ionic-strength blood environments without $\mathbf{B}(t)$ because of strong local electrostatic repulsion and further provide them with rich binding sites to load thrombolytic drugs via attractive electrostatic interactions (Fig. 1C). In addition, with the excellent affinity to AT III (Fig. 1D) (*44*, *45*), they may also show high self-anticoagulation while exhibiting low hemolysis and strong anti-bioadhesion because of the strong electrostatic repulsion (Fig. 1E) with constituents in blood environments, such as red blood cells (RBCs) and vascular endothelial cells (VECs). Moreover, under an external magnetic field, the MB@PSS NPs can be reversibly assembled into rod-like nanostructures due to the balance of magnetic attraction and electrostatic repulsion between them. These reversibly assembled rod-like nanostructures upon the application of an alternative magnetic field $\mathbf{B}(t)$ can work as swarming HPB-NRs. They can show strong driving forces and be collectively navigated to a targeted location due to their high magnetization and local hydrodynamic interactions.

With these integrated advantages, the MB@PSS NPs are injected into the bloodstream distal to the thrombus site, where they, in the form of well-dispersed individual particles, can be transported passively by the blood flow (Fig. 1F, Step-i), and subsequently collected using a permanent magnet placed at the upstream of the thrombus site with a blood flow velocity close to zero because of the flow blockage by the thrombus (Fig. 1F, Step-ii). Upon removal of the magnet and application of a precessing $\mathbf{B}(t)$, the swarming tissue-type plasminogen activator (t-PA)–loaded HPB-NRs are assembled from the t-PA–loaded MB@PSS NPs and start to crawl toward the thrombus near the blood vessel wall with minimized disturbance from the blood flow (Fig. 1F, Step-iii). During this process, all the building blocks of the HPB-NRs are not adhesive to the blood vessel wall due to the robust electrostatic repulsion between them. When approaching the thrombus, the swarming t-PA–loaded HPB-NRs are further actuated by a rotating $\mathbf{B}(t)$ to perform rotating motion and to penetrate the thrombus for synergistic thrombolysis using mechanical destruction and local drug release in the thrombus (Fig. 1F, Step-iv). In this way, the blood clots can be recanalized rapidly, and the HPB-NRs in the blood flow upon the removal of $\mathbf{B}(t)$ then automatically disassemble into dispersed individual NPs, allowing them to safely participate in circulation and be eventually removed from the body by metabolism (Fig. 1F, Step-v). Therefore, the as-constructed swarming magnetic HPB-NRs are envisioned to be biocompatible and can address the critical biosafety problem that occurred in the so far developed motile-targeting thrombolytic MNRs.

Characterization and robust dispersity of MB@PSS NPs in biological media

To construct biocompatible swarming magnetic nanorobots that can perform highly efficient thrombolysis with biosafety, we have first prepared MB@PSS NPs by an environment-friendly surface-initiated ATRP method (fig. S1) (*46*). As shown in Fig. 2A, the as-prepared MB@PSS NPs have an average size of 760 nm. In consideration of the size of the naked MBs (500 nm), a polymer shell of about 150 nm in thickness was wrapped on their surface. The polymer shell is a layer of PSS brushes, as suggested by the Fourier transform infrared (FTIR) spectrum in Fig. 2B in which the stretching vibration of the benzene ring skeleton can be found at 1426 cm^{-1}, and the strong broad peak from 1250 to 1000 cm^{-1}

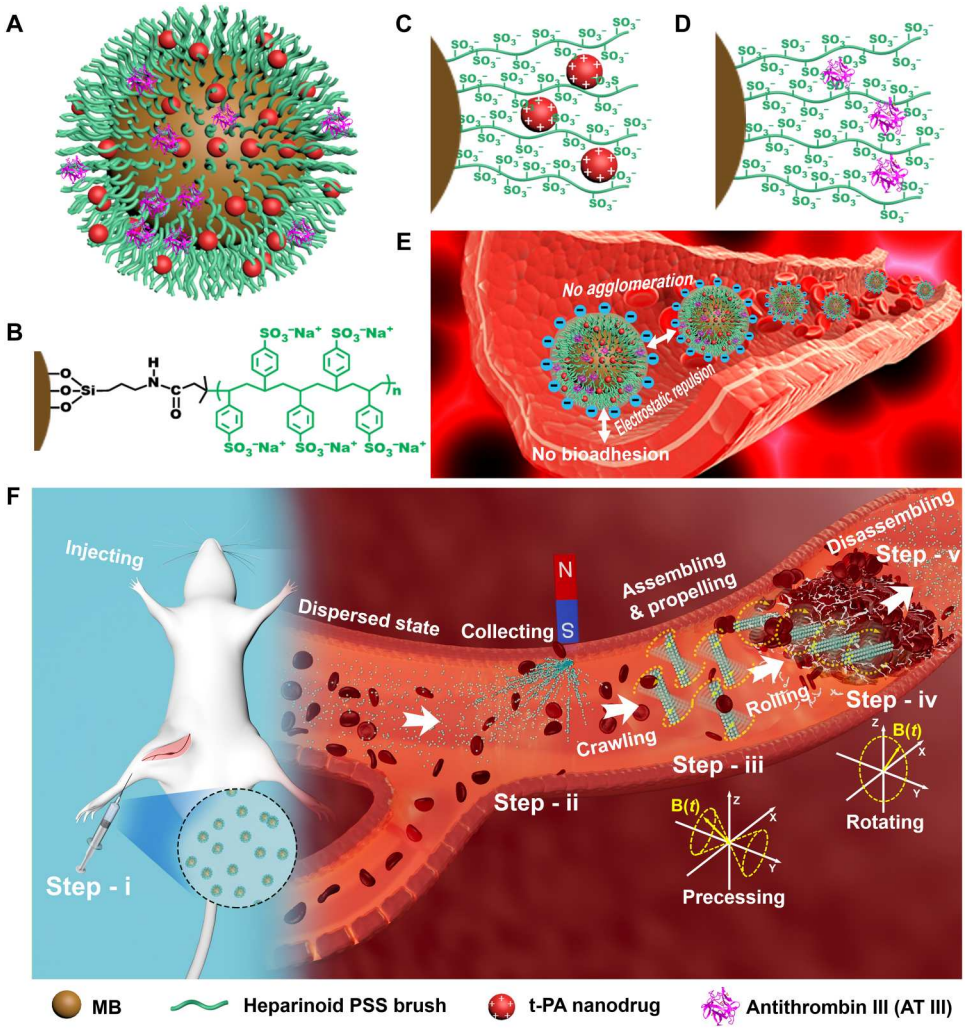

Fig. 1. Schemes illustrating the biosafety, drug loading, and targeted thrombolysis of swarming HPB-NRs based on MB@PSS NPs as building blocks. An individual MB@PSS NP with loaded drugs and conjugated AT III (**A**), a heparinoid-PSS brush (**B**), loading tissue-type plasminogen activator (t-PA) drugs (**C**), and conjugating AT III (**D**) with PSS brushes via high affinity. (**E**) Strong electrostatic repulsions among neighboring MB@PSS NPs and between MB@PSS NPs and vascular wall, ensuring their strong anti-agglomeration, anti-bioadhesion, and high biosafety in blood flows. (**F**) Safe and efficient targeted thrombolysis process by swarming HPB-NRs, including building block injection (Step-i), magnetic collection (Step-ii), nanorobot assembly/propulsion (Step-iii), thrombus destruction (Step-iv), and nanorobot disassembly (Step-v).

with a satellite at 1220 cm^{-1} belongs to -S=O symmetric stretching vibrations of -SO_3^- groups. The as-obtained MB@PSS NPs are superparamagnetic and have a saturation magnetization up to 33 emu g^{-1} (Fig. 2C). This suggests that the MB@PSS NPs have a strong magnetic attraction under external magnetic field and can serve as the building blocks of swarming magnetic nanorobots.

The MB@PSS NPs exhibit enhanced surface charge density (σ) and interparticle electrostatic repulsions in a high-ionic-strength solution, ensuring their stability and high dispersity in high-electrolyte biological media (Fig. 2D). This can be attributed to the notable shrinkage of quenched polyelectrolyte brushes with increasing the ionic strength (*47*), leading to the reduced shell thickness (*D*). As shown in Fig. 2E, increasing the NaCl concentration reduces the hydrodynamic size but increases the zeta potential (ζ) of the MB@PSS NPs. Both of them approach a constant value (780 nm for hydrodynamic size, −88.1 mV for ζ) when the NaCl concentration is over 50 mM. In contrast, ζ of naked colloidal particles in aqueous media sharply decreases with increasing the salt concentration (fig. S2). The increased ζ augments the interparticle electrostatic repulsion force F_1, as described in the following (*48*)

$$F_1 = \pi\varepsilon\zeta^2\kappa r e^{-\kappa d} \quad (1)$$

where κ^{-1} is the Debye-Hückel length, ε is the dielectric constant of the medium, and *d* is the interparticle surface-to-surface distance. In a medium with high ionic strength (*I*) of 150 mM (Fig. 2E), ζ of the MB@PSS NP was measured to be −88.1 mV, and κ^{-1} was estimated to be 0.79 nm according to its definition $\kappa^{-1} = (\varepsilon K_B T / 2000 N_A e^2 I)^{1/2}$, where K_B is Boltzmann's constant, *T* is the absolute temperature in kelvin, N_A is Avogadro's number, and *e* is the elementary charge. With the increased ζ, F_1 sharply increases as a function of ζ squared. Consequently, the MB@PSS NPs can be steadily

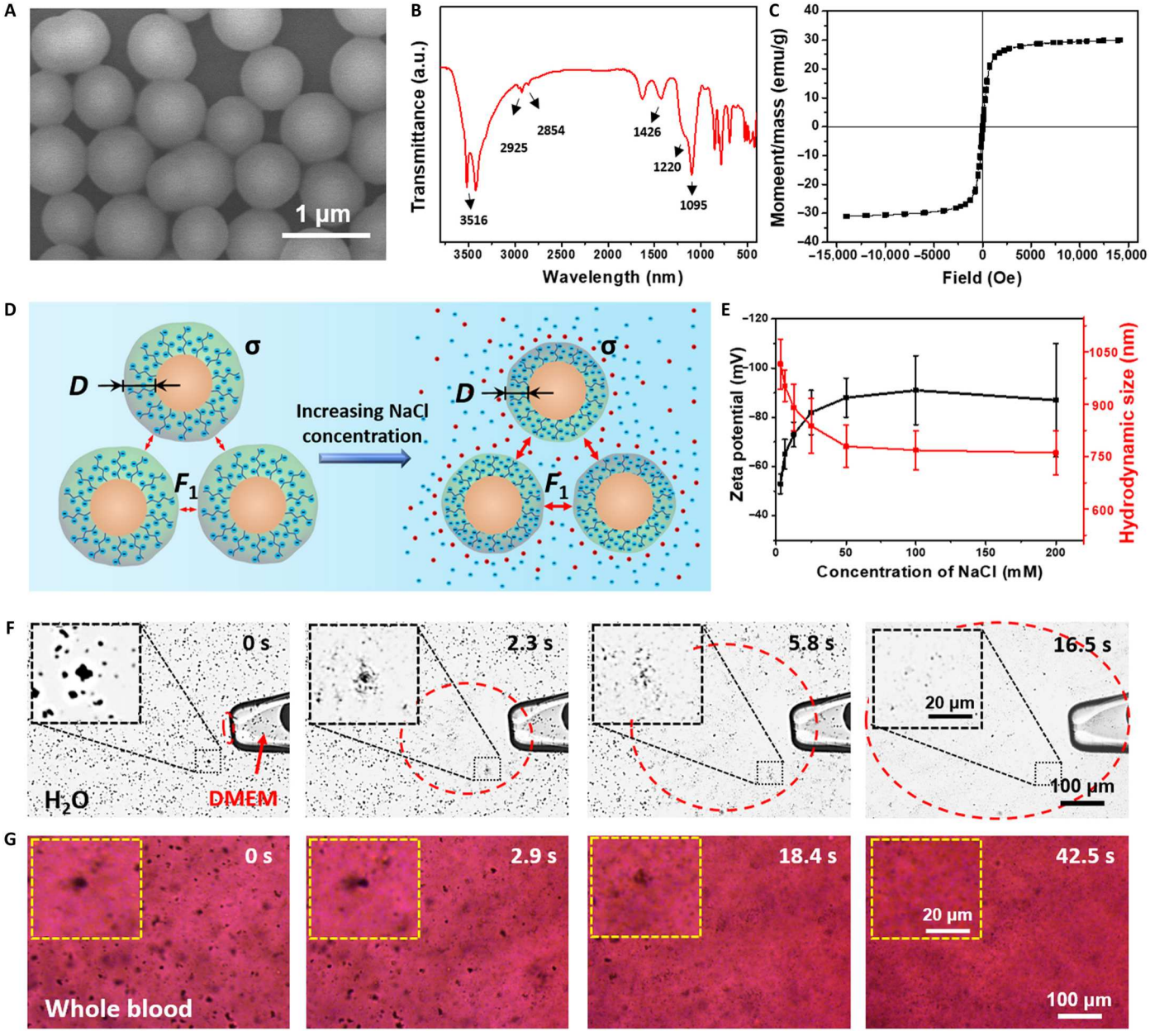

Fig. 2. Characterization and dispersity of MB@PSS NPs in biological media. (**A** to **C**) SEM image (A), FTIR spectrum (B), and magnetic hysteresis loop (C) of the MB@PSS NPs. a.u., arbitrary units. (**D**) Schematic diagram illustrating the enhanced surface charge density (σ) and interparticle electrostatic repulsion (F_1) of MB@PSS NPs in biological media due to the shrinkage of PSS brush shell thickness (D) with the increased electrolyte concentration (C_e). (**E**) ζ and hydrodynamic size of the MB@PSS NPs in an aqueous solution with different NaCl concentrations. (**F** and **G**) Time-lapse microscopic images depicting the dispersion of agglomerated MB@PSS NPs in an aqueous suspension upon injecting DMEM, where the red dashed circles indicate the DMEM diffusion range (F) or being dropped into whole blood (G). The left-upper inserts are partially magnified microscopic images.

dispersed without agglomeration in high-electrolyte biological media.

As shown in Fig. 2F and movie S1, the agglomerated MB@PSS NPs in an aqueous suspension gradually disperse into individual particles upon the injection of Dulbecco's modified Eagle's medium (DMEM). With DMEM diffuses continuously, the area where MB@PSS NPs disperse expands correspondingly, as indicated by the red dashed circles. In contrast, naked MBs are dispersed in water but become agglomerated in DMEM because of the charge screening effect (fig. S3). In addition, the MB@PSS NPs show excellent dispersity in blood and serum. As shown in Fig. 2G and movie S2, when an aqueous suspension of MB@PSS NPs is dropped into the blood, the MB@PSS NPs will gradually disperse into single particles within 42.5 s. Similarly, the MB@PSS NPs also have good dispersity in serum (fig. S4 and movie S3). These results indicate that the MB@PSS have no risk of secondary thrombosis from HPB-NRs themselvesin the blood system.

Magnetic propulsions in blood environments

When subjected to a precessing or rotating magnetic field $\mathbf{B}(t)$, magnetic NPs tend to self-assemble into wobbling or rotating rods. As shown in fig. S5A, the self-assembly of charged magnetic NPs under the magnetic field is mainly governed by the balance of electrostatic repulsion F_1, van der Waals force (F_2) (*49*), and magnetic dipole-dipole attraction (F_3) (*48*). In the case of the MB@PSS NPs that have a high ζ in high-electrolyte media, they tend to approach each other at a d greater than the equilibrium separation distance (d_0, ~2.5 nm) due to the negative ΣF at $d > 2.5$ nm and reach an equilibrium at d_0, where $\Sigma F = 0$ (fig. S5B). Because of the dominant electrostatic interparticle repulsion ($F_1 >> F_2$), the assembled MB@PSS NPs (or HPB-NRs) will promptly disassemble into dispersed particles upon removal of the applied $\mathbf{B}(t)$ ($F_3 = 0$). In contrast, the naked MBs have a low ζ (−1.4 mV at a C_e of 150 mM), resulting in weak F_1 and persistent negative ΣF. They tend to closely pack with one another ($d_0 \rightarrow 0$) (fig. S5C), leading to their easy agglomeration in high-electrolyte biological media during magnetic self-assembly.

Once assembled, the HPB-NRs are capable of performing crawling or rolling motion under the applied precessing or rotating $\mathbf{B}(t)$ (Fig. 3A). During the crawling motion, the two ends of the rod-like HPB-NRs alternatively touch a substrate surface when rotating around the precessing axis. With a hydrodynamic no-slip boundary near the substrate (e.g., blood vessel wall), the two precessing ends exhibit different hydrodynamic mobility based on their distance from the substrate surface, thereby enabling the HPB-NRs to perform translational kayaking (crawling) motion (*50*). As shown in Fig. 3B and movie S4, under a precessing $\mathbf{B}(t)$ with B_0 of 10 mT and f of 5 Hz, the MB@PSS NPs self-assemble into short rod-like structures (i.e., nanorobots) (0 to 2.5 s; Fig. 3B) and then "crawl" on the substrate in a kayaking motion behavior (2.5 to 15.0 s; Fig. 3B). All assembled rod-like structures crawl in a synchronized manner and move in a well-defined collective orientational order (red trajectories in Fig. 3B). When the precessing $\mathbf{B}(t)$ is changed into a rotating one (rotating in the X-Z plane), they perform collective motions in a "rolling" mode (15.0 to 20.1 s in Fig. 3B). When $\mathbf{B}(t)$ is removed, the nanorobots stop moving and gradually disassemble into dispersed individual particles again (20.3 to 46.8 s, Fig. 3B). This indicates that the HPB-NRs can reversibly transform between dispersed individual particles and assembled nanorod-like structures with collective motions in response to $\mathbf{B}(t)$.

In addition, by adjusting the applied $\mathbf{B}(t)$ (fig. S8 and movie S5), the swarming HPB-NRs can perform dynamic reconfigurations, transforming from vortexes to "crawling" rods, vortexes to rolling wheels, long crawling rods to short ones, and dispersed NPs, respectively. By adjusting $\mathbf{B}(t)$, the speed and direction of the swarming HPB-NRs can be controlled. As shown in Fig. 3C, the crawling HPB-NRs can move up to 267 μm s^{-1}. The rolling HPB-NRs walk slower than the crawling ones and exhibit a maximum v of 197 μm s^{-1}. When f is increased from 2 to 80 Hz, the swing angle of the crawling HPB-NRs gradually decreases from 116° to 0° (fig. S6 and movie S6). As shown in fig. S7 and movie S7, the nanorobot can move in a predetermined U-shaped trajectory with multiple turns by adjusting the precession axis of $\mathbf{B}(t)$.

As shown in Fig. 3D, the nanorobot can also crawl in blood. It can push RBCs away once one end touches them, therefore leaving a clear track of "footprints" on the substrate. Figure S9 indicates that the kayaking motion speed (v) of the HPB-NRs under the precessing $\mathbf{B}(t)$ in serum, plasma, and whole blood can reach 130, 119, and 49 μm s^{-1}, respectively. The decreased v in blood environments compared to that in the culture medium (DMEM, 255 μm s^{-1}) is attributed to the high viscosity of these media (~0.7, ~1.6, ~1.9, and 4 to 5 mPa·s for DMEM, serum, plasma, and whole blood, respectively).

The HPB-NRs can adapt to blood environments. As the building blocks, MB@PSS NPs, have a high density of surface charges in high-electrolyte biological media, the HPB-NRs in serum can disassemble into dispersed particles when $\mathbf{B}(t)$ is removed (Fig. 3E and movie S9). This implies that the HPB-NRs can avoid vascular occlusion by themselves. In addition, as shown in Fig. 3F and movie S10, a swarm of the HPB-NRs could crawl on a simulated inner wall of blood vessels, VECs grown on a glass substrate. This suggests that the HPB-NRs can perform crawling locomotion on blood vessel walls, like leukocytes (*51*). Moreover, no adhesion of MB@PSS NPs to the surface of VECs or particle loss was observed because of their strong repulsions with such surface, revealing no risk of potential vascular occlusion. Meanwhile, the cell viability of VECs is over 95% when exposed to HPB-NRs with a concentration of 100 μg ml^{-1} (fig. S10). This proves that the HPB-NRs have a low cytotoxicity to VECs.

Heparinoid brush length effect on blood-environment compatibility

The length of surface heparinoid-PSS brushes (L_{PSS}) of the MB@PSS NPs, which can be controlled by simply changing the ATRP time (t) (*46*), has an important impact on the performance of the swarming magnetic HPB-NRs in biological media, such as antiadhesion and anticoagulation performances. As shown in Fig. 4A, the hydrodynamic size of the MB@PSS NPs almost linearly increases from 500 to 1127 nm with t. This is also verified by the scanning electron microscopy (SEM) images in fig. S11.

With surface heparinoid-polyelectrolyte PSS brushes, the MB@PSS NPs and HPB-NRs have low hemolysis. As indicated in Fig. 4B, naked MBs show a high hemolysis rate of 12.1%. In contrast, the MB@PSS-t NPs have a low-level hemolysis (<5%), suggesting that the MB@PSS NPs are highly hemocompatible (*52*), and have a negligible influence on the damage of RBCs. For the typical MB@PSS NPs (i.e., MB@PSS-6 NPs), they only have a low hemolysis rate of 3.6%, and the HPB-NRs assembled from them under $\mathbf{B}(t)$ still demonstrate a hemolysis rate of 4.8% (fig. S12). The slight increase in the hemolysis rate after magnetic actuation is attributed to the possible rupture of trace RBCs caused by the mechanical forces of HPB-NRs. Surface properties of colloidal particles, such as surface chemistry, charge density, and wettability, are critical for their blood compatibility (*45*). The MB@PSS NPs contain rich surface -SO_3^- groups bearing a high density of negative charges (*53*), which generate repulsion to RBCs (−15 mV in ζ). Thus, they can prevent hemolysis.

With surface hydrophilic negatively charged PSS brushes, the HPB-NRs assembled from MB@PSS NPs would avoid random adhesion to the substrate when they are collectively driven under $\mathbf{B}(t)$. The statistical results in Fig. 4C indicate that the adhesion rate of the HPB-NRs to the substrate decreases with increasing L_{PSS}. When L_{PSS} reaches 249 nm (corresponding to that of MB@PSS-6 NPs), the MB@PSS NPs rarely adhere to the substrate. As depicted in Fig. 4D and movie S11, MB@PSS-6 can freely move on a glass substrate almost without adhesion-caused particle loss in DMEM,

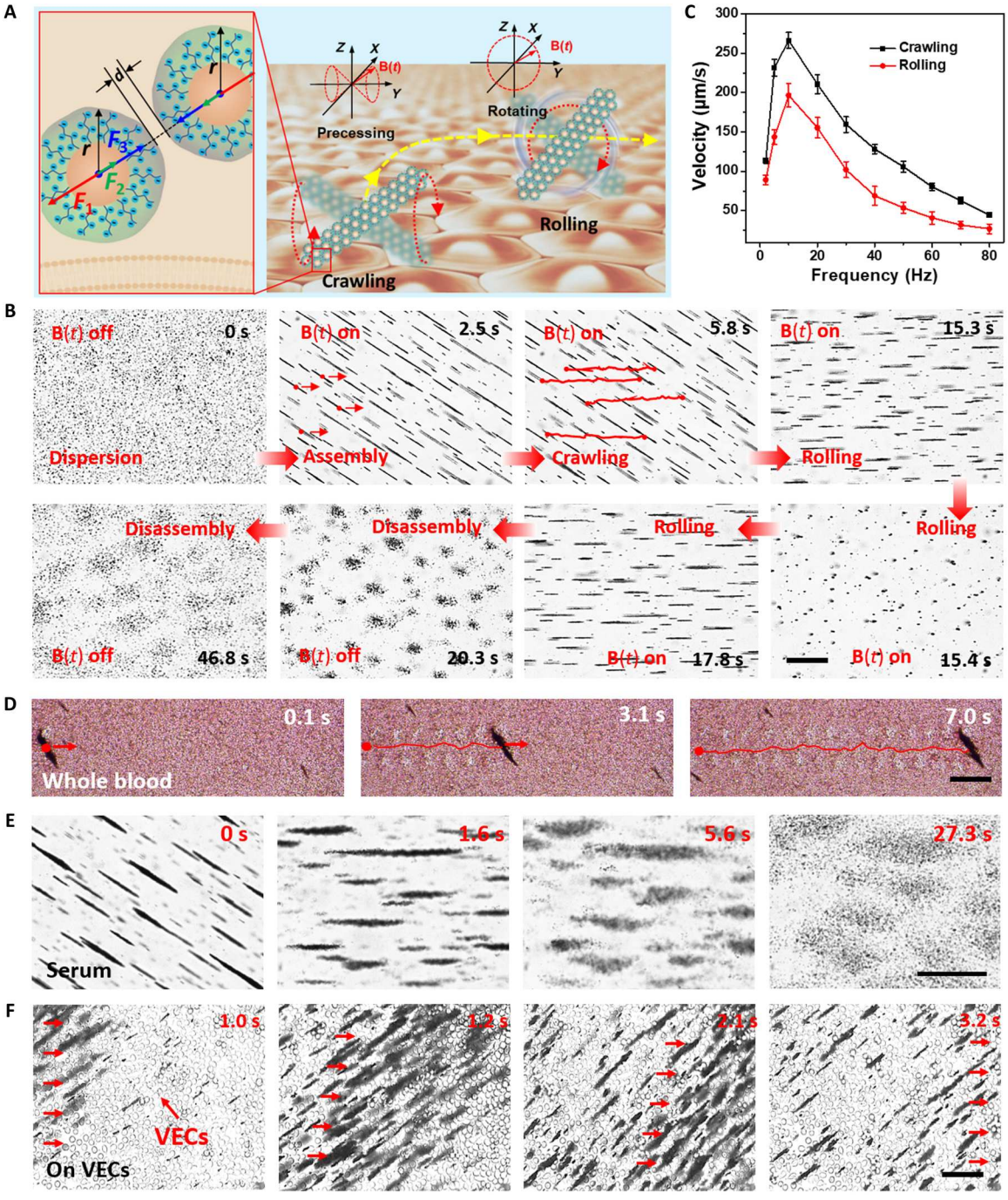

Fig. 3. Magnetic propulsion and blood-environment adaptivity of magnetic HPB-NRs. (**A**) Schematic diagram of the kayaking (crawling) and rolling motion of a rod-like HPB-NR assembled from the MB@PSS NPs under a precessing or rotating **B**(*t*). F_1, F_2, and F_3 represent the electrostatic repulsion, van der Waals force, and magnetic dipolar attraction between two neighboring MB@PSS NPs at a specific interparticle distance (*d*), respectively. (**B**) Reversible assembly and magnetically driven propulsions (crawling and rolling propulsions) of the HPB-NRs in the culture medium (DMEM) in response to a precessing or rotating **B**(*t*). B_0 and *f* of the precessing or rotating **B**(*t*) are 10 mT and 5 Hz, respectively. Scale bars, 80 μm. (**C**) Average velocity (*v*) versus *f* for the crawling and rolling HPB-NRs. (**D**) Magnetic propulsions of the HPB-NRs in whole blood. (**E**) Disassembly of the HPB-NRs in serum after **B**(*t*) is removed. (**F**) Crawling motion of the HPB-NRs on a dense layer of VECs. Scale bars, 100 μm (D to F).

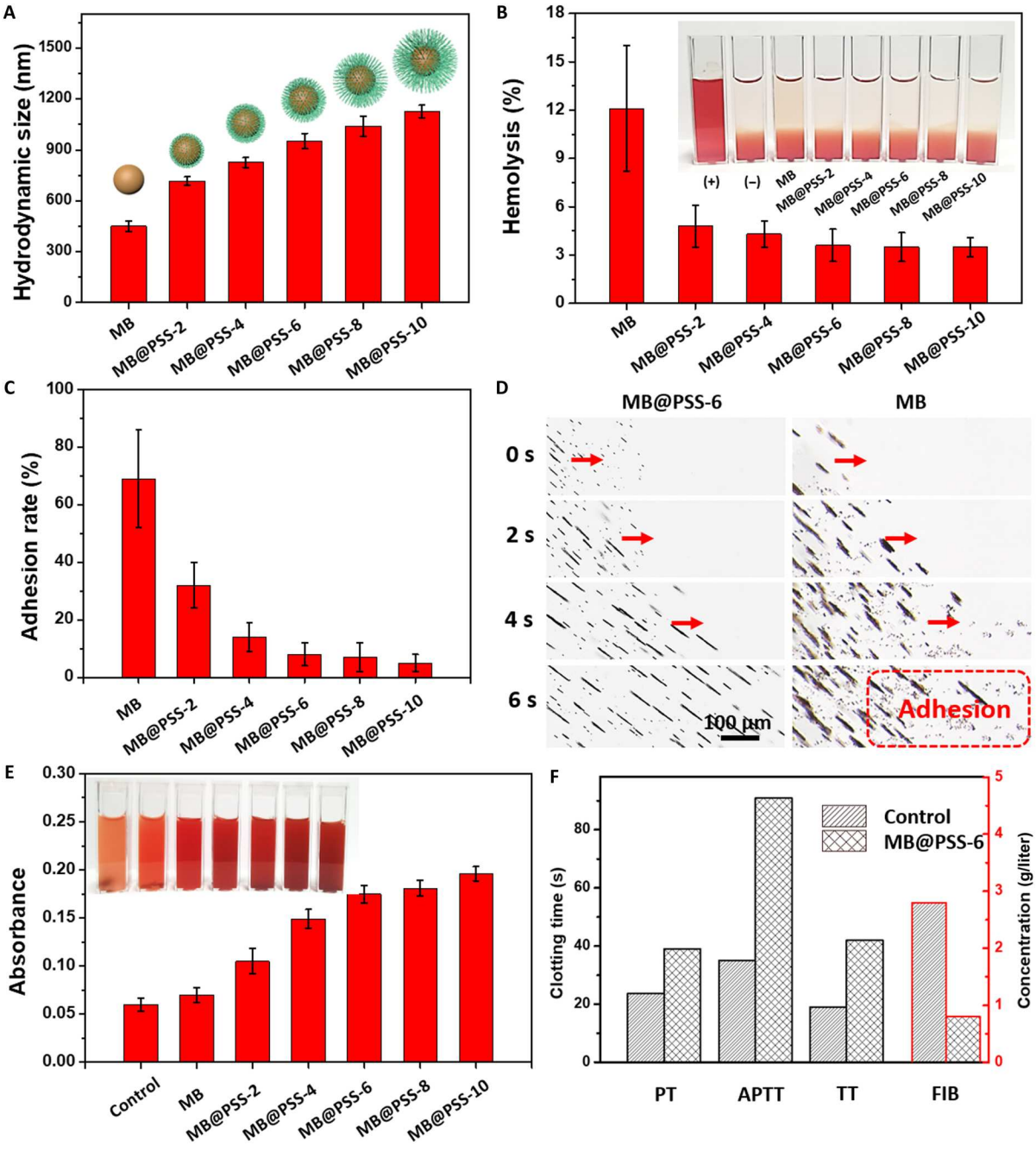

Fig. 4. Heparinoid-PSS brush length effect on blood-environment compatibility of MB@PSS NPs. (**A**) Hydrodynamic sizes of the MB@PSS NPs obtained at different polymerization time (*t* in a unit of hours), MB@PSS-*t*. (**B**) Hemolysis and digital photographs (insets) of RBCs after being exposed to the naked MBs and MB@PSS-*t* NPs. PBS (−) and deionized water (+) were used as negative and positive controls, respectively. (**C**) Adhesion (or particle loss) rate of the naked MBs and MB@PSS-*t* to the substrate when the NRs assembled from them collectively move in DMEM. (**D**) Optical microscopic images illustrating the magnetic propulsions of the NRs assembled from MB@PSS-6 (left) and naked MBs (right) in DMEM, revealing that the adhesion and particle loss to the substrate occur with the naked MBs but disappear for MB@PSS-6 NPs. Scale bar, 100 μm. (**E**) Anticoagulation performance of naked MBs and MB@PSS-*t* NPs evaluated by hemoglobin content in the supernatant. The absorbance of saline is used as the control. (**F**) In vitro anticoagulation activities of naked MBs (control) and MB@PSS-6 NPs.

while those from the NRs assembled from naked MBs undergo a serious particle loss. This can be explained by the strong repulsion between MB@PSS NPs and the substrate even at a high electrolyte concentration due to the counterion osmotic pressure and the hydration layer surrounding the charged polymer segments (*54*, *55*).

Moreover, the MB@PSS NPs are able to inhibit coagulation factors and to show good self-anticoagulation ability. As shown in Fig. 4E, the anticoagulation ability of the MB@PSS NPs increases accordingly with increasing L_{PSS}. MB@PSS-6 shows an anticoagulation ability more than two times higher than naked MBs. This is because increasing L_{PSS} enlarges the content of the surface -SO_3^- groups, which bind more AT III to inhibit the blood clotting cascade (*44*, *56*) and coagulation factors. We evaluated the anticoagulation effect of the MB@PSS-6 NPs in vitro by measuring the activated partial thromboplastin time (APTT), prothrombin time (PT), thrombin time (TT), and fibrinogen (FIB) concentration with those of naked MBs as control experiments to reflect the endogenous and exogenous coagulation pathways (*56*), as well as the clotting process (*57*). As depicted in Fig. 4F, the APTT experiences a substantial increase from 35.1 to 91.0 s (nearly three times), and the TT increases from 19.0 to 42.1 s when comparing the system with MB@PSS NPs to that of naked MBs. Similarly, the PT of the system with MB@PSS NPs was also prolonged compared to that with naked MBs. The FIB concentration, which is inversely related to clotting time, in the plasma with MB@PSS NPs is 0.80 g/liter, much lower than that with naked MBs (2.83 g/liter). This implies that the MB@PSS NPs can to some extent act as anticoagulants in the plasma and ultimately reduce FIB concentration. Thus, the endogenous and exogenous coagulation of the HPB-NRs can be largely inhibited due to the surface PSS brushes. These results suggest that the HPB-NRs are compatible with blood environments.

In vitro thrombolysis

Besides the excellent blood-environment compatibility, the swarming HPB-NRs can efficiently perform thrombolysis therapy after loading thrombolytic drugs (t-PA) in the building blocks of MB@PSS NPs. As shown in fig. S13, the MB@PSS NPs can be densely loaded with t-PA by electrostatic attraction when t-PA was previously coated by ε-polylysine (PL) to form drug nanospheres of about 37 nm in size. The loading capacity was confirmed to be 123.6 mg t-PA/g MB@PSS using a bicinchoninic acid (BCA) protein kit (fig. S14). The activity of as-loaded t-PA can maintain over 90% within 1 hour and gradually decrease to 46% after 4 hours (fig. S15A). Before magnetic actuation, the MB@PSS NPs could only release about 15% of the loaded t-PA in 4 hours. When the rotating $\mathbf{B}(t)$ was applied, they released over 50% of the loaded t-PA before reaching the equilibrium at about 2 hours (fig. S15B). This suggests that the release of t-PA in the as-loaded MB@PSS NPs can be magnetically controlled. The MB@PSS NPs without actuation only release t-PA through passive diffusions or osmosis transportation under concentration gradients, while they upon the application of $\mathbf{B}(t)$ are assembled into magnetic HPB-NRs, which perform rotating motions to enhance the mass exchange, accelerating the release of t-PA (*58*).

A microfluidic chip (microchannel width of 500 μm and depth of 200 μm) was designed to visualize the thrombolysis by the HPB-NRs (Fig. 5, A and B, and movie S12). Under the magnetic actuation and navigation, a swarm of t-PA–loaded HPB-NRs passes through the microchannel and moves toward a thrombus placed in a microwell by their kayaking-like crawling motions (0 to 12.1 s in Fig. 5A) and then penetrates the thrombus using their rolling motions (30.4 to 160.2 s in Fig. 5A and fig. S16). The subsequent thrombolysis process by the t-PA–loaded nanorobots can be clearly observed under an optical microscope (Fig. 5B). In the thrombolysis process, the HPB-NRs released t-PA locally near or in the thrombus under a rotating $\mathbf{B}(t)$, and the thrombus was almost dissolved after 3.5 hours of treatment.

After the visual observation of the thrombolysis by the HPB-NRs, their thrombolytic efficacy was further quantitatively evaluated in vitro. Except for the control group, the supernatant color change and the thrombus size reduction were observed in the other four groups, suggesting the occurrence of thrombus dissolution (Fig. 5C). The obvious thrombus dissolution in the moving HPB-NRs [NRs + $\mathbf{B}(t)$] group suggests that the mechanical force of nanorobots can have a thrombolytic effect. The supernatant color in the moving t-PA–loaded HPB-NRs [NRs + t-PA + $\mathbf{B}(t)$] group is much darker than that in other groups. As shown in the quantitative results of Fig. 5D, the NRs + t-PA + $\mathbf{B}(t)$ group has the highest concentration of the released fibrin and hemoglobin from the blood clot, further verifying the strongest thrombolytic effect of the swarming t-PA–loaded HPB-NRs. Figure 5E indicates that the NRs + t-PA group demonstrates a higher thrombolysis rate (ϕ_t) than the t-PA group. This implies that the affinity of t-PA to thrombus components is stronger than that to PSS brushes, and the loaded t-PA molecules on the MB@PSS NPs can effectively diffuse out of PSS brushes. Furthermore, the loaded t-PA has a short average diffusion length compared to free t-PA as the former can directly contact with the thrombus under gravity. ϕ_t in the NRs + t-PA + $\mathbf{B}(t)$ group is higher than the sum of that in NRs + $\mathbf{B}(t)$ and NRs + t-PA groups, suggesting a synergistic effect from mechanical destruction and targeted drug dissolution in thrombolysis of the moving t-PA–loaded HPB-NRs. This synergistic effect can be rationalized by the combination of the enhanced diffusion and release of t-PA with the mechanical destruction of the swarming t-PA–loaded HPB-NRs. At first, the percentage of t-PA released from the moving t-PA–loaded HPB-NRs (over 50%) can be magnetically enhanced, surpassing that observed from immotile t-PA–loaded MB@PSS NPs (15%). This increases the local availability of t-PA. Second, the rolling HPB-NRs can penetrate into the thrombus under a rotating $\mathbf{B}(t)$ via mechanical destruction and further promote the delivery of the t-PA locally inside the thrombus. This improves the transfer and utilization of t-PA. With these two effects, the swarming t-PA–loaded HPB-NRs can perform thrombolysis more efficiently than the combination of swarming HPB-NRs and immobile t-PA–loaded MB@PSS NPs.

In vivo thrombolysis

To investigate the targeted thrombolysis of the HPB-NRs in vivo, we established a Sprague-Dawley (SD) rat's femoral vein venous thrombus model. The experimental setup for the thrombolysis treatment is shown in Fig. 6A. The femoral vein venous thrombus was prepared using the $FeCl_3$ injury method as reported (*59*). When the thrombus was generated, the blood flow in the model vessel was blocked (Fig. 6B and movie S13), which would prevent MNRs or thrombolytic drugs from reaching the thrombus site. After the construction of the femoral vein thrombus model, the rats were injected with the magnetic MB@PSS NPs distal to the femoral vein thrombosis. As shown in Fig. 6C and movie S14, a significant

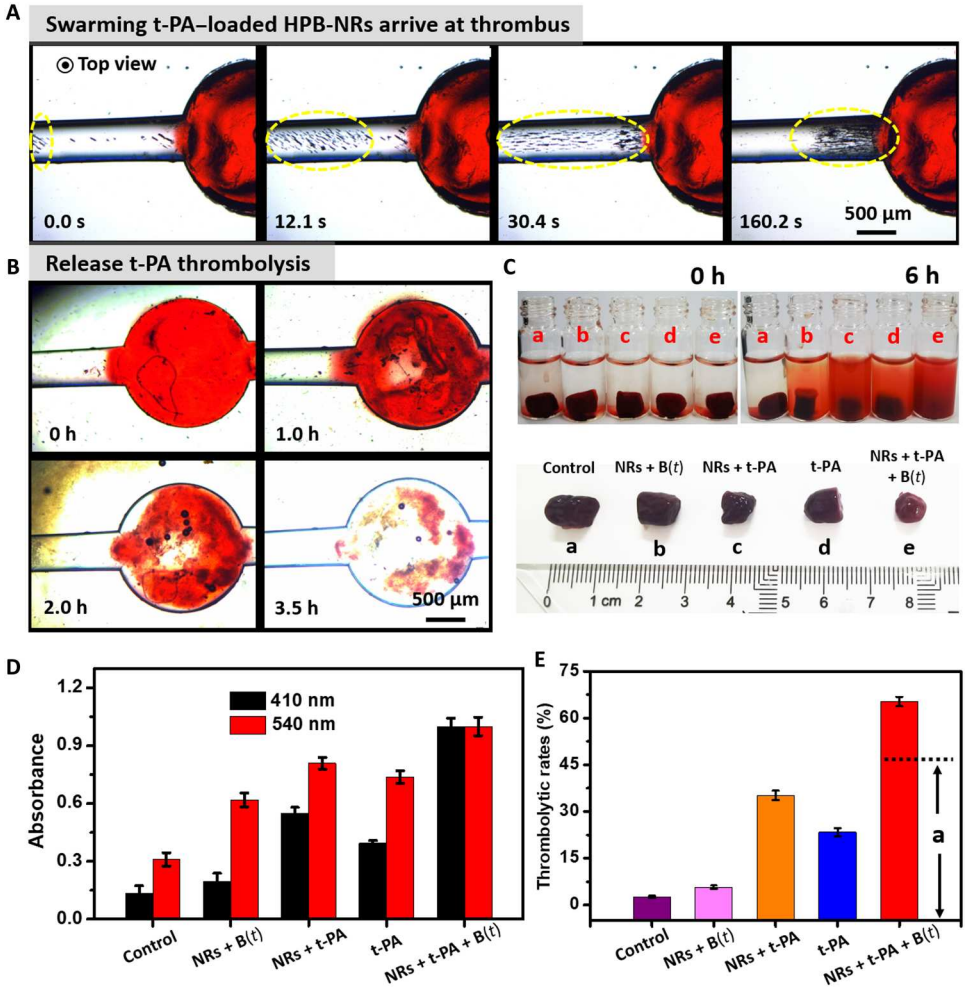

Fig. 5. Targeted thrombolysis in vitro. (**A**) Time-lapse microscopic images depicting the propulsion of the swarming t-PA–loaded HPB-NRs toward a thrombus under **B** (*t*) from the top view. (**B**) Targeted thrombolysis by the swarming t-PA–loaded HPB-NRs. (**C**) Digital photographs of blood clots after being exposed to control (saline), moving HPB-NRs [NRs + **B**(*t*)], immobile t-PA–loaded MB@PSS NPs (NRs + t-PA), t-PA, and moving t-PA–loaded HPB-NRs [NRs + t-PA + **B**(*t*)] for 6 hours. (**D**) Optical absorbance of the supernatant at 410 and 540 nm (OD_{410} and OD_{540}), corresponding to the indicators of the released fibrin (410 nm) and hemoglobin (540 nm) from the blood clots shown in (C) after 6-hour treatment, respectively. (**E**) Calculated thrombolytic rate by weighting the mass of the thrombus after 6-hour treatment, where (a) in group NRs + t-PA + **B**(*t*) represents the simple sum of the separate thrombolytic rates contributed from the mechanical force and the targeted t-PA.

enhancement of the acoustic intensities was observed, suggesting the accumulation of the MB@PSS NPs near the thrombus site by the magnetic collection.

The therapeutic effects of different administration groups over time are shown in Fig. 6D, all treatment groups have a thrombolytic effect except the control (saline) group, but the thrombolysis trends are different. The NRs + **B**(*t*) group only displays a slight increase in the blood flow signal after a 4-hour treatment and so does the t-PA group. The former suggests that the mechanical force alone is too weak to cause serious damage to the thrombus, while the latter manifests a low drug utilization rate due to the lack of targeting ability. In contrast, the NRs + t-PA group has an obvious blood flow signal after a 4-hour treatment due to the targeted delivery of the t-PA. More appealingly, the NRs + t-PA + **B**(*t*) group clearly exhibits rapid thrombolysis compared to the other three groups.

The quantitative analysis of the blood flow in Fig. 6E indicates that the blood flux in all treatment groups gradually increases over time except for the control group. Among them, the NRs + t-PA + **B**(*t*) group shows the maximum increment in blood flux, which is higher than the sum of that in NRs + **B**(*t*) and NRs + t-PA groups, confirming that the in vivo thrombolysis by the swarming HPB-NRs also demonstrates a synergistic effect from the targeted t-PA delivery and mechanical destruction, consistent with the in vitro thrombolysis experiments. The synergistic thrombolysis performance of the NRs + t-PA + **B**(*t*) group is also observed by measuring the residual thrombus area after different treatments, as depicted in Fig. 6F. The above in vivo thrombolysis results clearly confirm that the swarming t-PA–loaded HPB-NRs can effectively dissolve the thrombus in the femoral vein. As the swarming HPB-NRs can be reversibly switched into well-dispersed individual NPs without **B**(*t*) in serum (Fig. 3E), this motile targeted platform may have no risk of secondary thrombosis from HPB-NRs themselves.

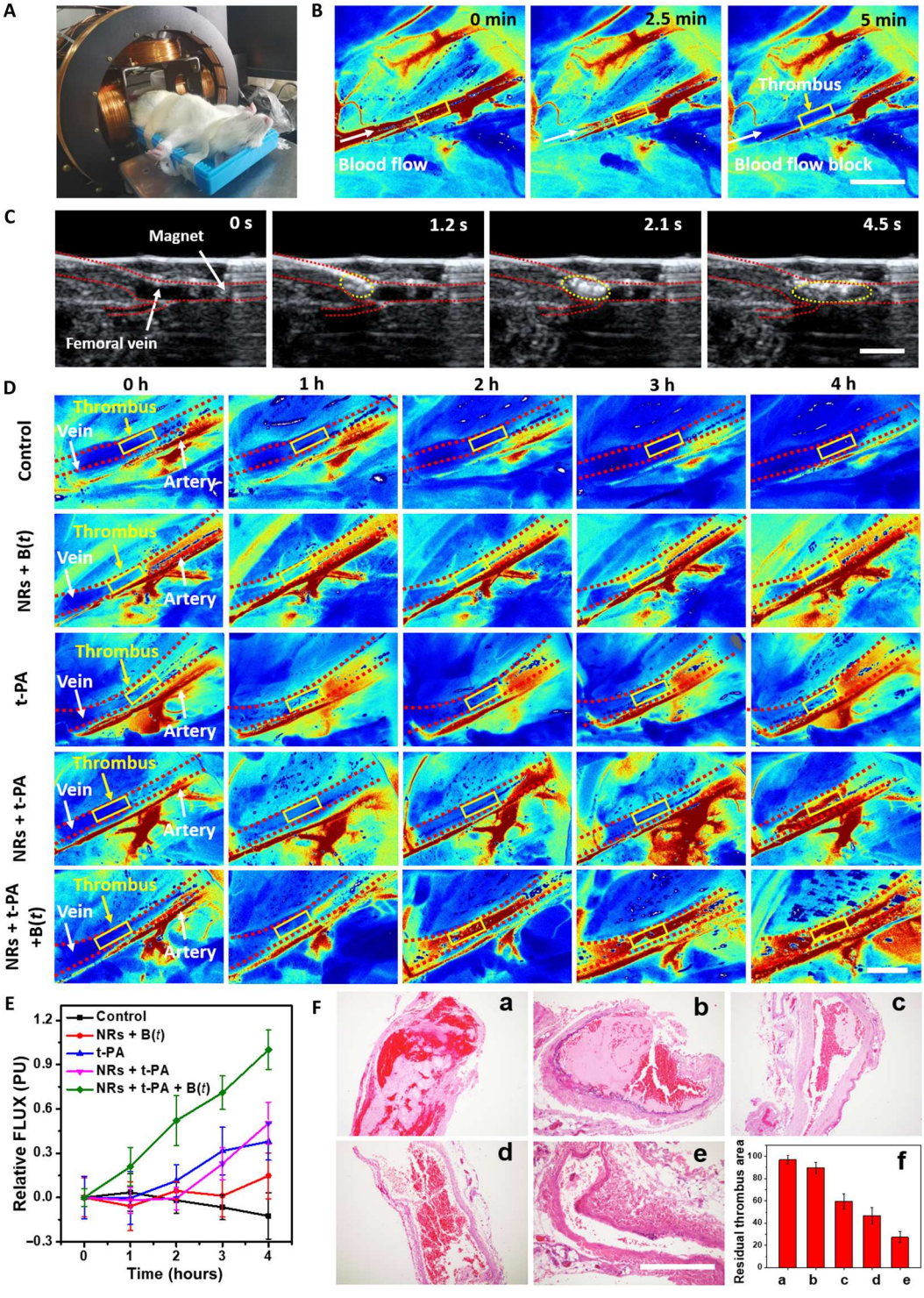

Fig. 6. Targeted thrombolysis in vivo. (**A**) Experimental setup of the targeted thrombolysis treatment of SD rat's femoral vein venous thrombus in vivo by the swarming HPB-NRs. (**B**) Blood flow in the SD rat's femoral vein monitored by the LSBFMS before (0 min) and after (2.5 and 5 min) the thrombus is generated. Scale bar, 5 mm. (**C**) Real-time tracking of the MB@PSS NPs in the SD rat's femoral vein by ultrasound imaging when the MB@PSS NPs are magnetically collected near the thrombus by a permanent magnet. Scale bar, 2 mm. (**D**) LSBFMS-monitored blood flow in the femoral vein of the SD rats from the control (saline), NRs + **B**(*t*), t-PA, NRs + t-PA, and NRs + t-PA + **B**(*t*) groups at different time. Scale bar, 4 mm. (**E**) Blood perfusion over time for all groups ($n = 5$ per group). (**F**) Representative H&E staining photomicrographs of the femoral vein venous thrombus after 4-hour treatment of control (a), NRs + **B**(*t*) (b), t-PA (c), NRs + t-PA (d), NRs + t-PA + **B**(*t*) (e), as well as the corresponding residual thrombus area (f). Scale bar, 1 mm.

Biological safety

For an injectable MNRs working in the blood circulation system, its safety evaluation is vital, which, however, is currently limited to the histological analysis. Here, we have conducted an overall safety evaluation, including a comprehensive blood biochemistry panel, histological analysis, and biodistributions over the building blocks of the HPB-NRs (MB@PSS NPs) with naked MBs as a control. Figure 7 shows the results after 2 and 14 days of injecting the building blocks of the HPB-NRs (MB@PSS NPs) into the blood vessel of mice. During the observation period, no mouse died after being intravenously administrated with MBs or MB@PSS NPs. They were emotionally stable, and no inflammatory reactions or necrosis were observed in any of the mice. The blood biochemistry analysis (Fig. 7A) shows that the MB@PSS NPs show no hepatic and renal toxicity, as verified by the fact that the mice injected with MB@PSS NPs had similar levels in hepatic toxicity markers [alanine transaminase (ALT), aspartate aminotransferase (AST), total bilirubin (TBIL), albumin (ALB), total protein (TP), and globulin (GLOB)] and renal toxicity markers [urea and creatinine (CREA)] to those in the control group. In contrast, the mice administrated with naked MBs (without PSS brushes) show an elevation in TBIL after 14 days, indicating liver damage. In addition, the hematoxylin and eosin (H&E)–stained slices of the heart, liver, spleen, lung, and kidney of the mice injected with naked MBs and MB@PSS NPs were collected. As shown in the histological images (Fig. 7B and fig. S17), no obvious pathological change or inflammatory lesion appears in both short-term (2 days) and long-term (14 days) periods.

The biodistributions of the MB@PSS NPs in the mice were investigated in detail at 14 days. As shown in Fig. 7C, the MB@PSS NPs mainly existed in the liver and spleen. This is because liver and spleen are usually the dominant organs for clearance of NPs from bloodstream. All the MB@PSS NPs existing in these organs are phagocytized by immune cells (marked with a yellow dotted wireframe in Fig. 7C), indicating that they will be excreted from the body eventually. In stark contrast, the MBs existing in the liver and spleen are mainly in the form of aggregates, which are difficult to be phagocytized by immune cells and may cause damages to these organs in long term. This suggests that the heparinoid-PSS brushes on the surface of MB@PSS NPs play a crucial role in the dispersity of them in the blood environment. The swarming magnetic nanorobots based on MB@PSS NPs show excellent biological safety, and they are believed to have a potential for the clinical application of thrombolysis. The findings presented in Fig. 7 emphasize that relying solely on histological analysis is inadequate for a thorough assessment of the biological safety of injectable thrombolytic nanorobots operating within the bloodstream. A comprehensive understanding of their biological safety should at least encompass a blood biochemistry panel, histological analysis, and biodistribution studies.

DISCUSSION

Thrombotic occlusions of blood vessels will cause severe tissue damage or even organ failure, leading to life-threatening cardiovascular disorders, such as myocardial infarction, ischemic stroke, and venous thromboembolism (*60*–*63*). They are diagnosed most limited to the late stages and thus only have a narrow therapeutic window. The most widely used clinical treatment of thrombus is systemic administration of thrombolytic drugs, which, however, suffer from a short half-life, inactivation, low bioavailability, off-target side effects (allergic reactions and unwanted tissue hemorrhage), and limited thrombus penetration (*62*, *64*, *65*). With unique propulsions in liquid media, MNRs may accelerate drug diffusion or perform targeted thrombolysis by directly delivering thrombolytic drugs to a thrombus (*32*). However, the catalytically propelled and light-driven MNRs usually demonstrate sluggish thrust and only perform locomotion at a single-bot level in high-ionic-strength biological environments. They have to experience a long time to accumulate at the thrombus clot and exhibit low therapeutic efficacy in thrombolysis (*15*, *66*). Thus, they are not ideal for time-critical thrombolysis therapy, especially for acute thrombotic diseases. On the other hand, the so far developed swarming magnetic MNRs that can load thrombolytic drugs (including t-PA, urokinase plasminogen activator, heparin, and streptokinase) may suffer from serious agglomeration and random bioadhesion in high-ionic-strength blood environments. Thus, when performing in vivo thrombolysis, they have enormous risks, such as systemic toxicity and secondary embolization, far from clinical applications (*67*). In this study, by developing superparamagnetic NPs elaborately grafted heparinoid-PSS brushes as building blocks, we have constructed biocompatible swarming magnetic nanorobots that can be reversibly transformed into individually dispersed NPs without magnetic field and can collectively move in the blood flow without adhesion to vascular walls upon the application of $\mathbf{B}(t)$. They can perform safe and efficient targeted thrombolysis in vivo via synergistic effects of mechanical destruction and targeted drug delivery.

For in vivo biomedical applications of MNRs, especially for injectable MNRs working in blood systems, safety is a priority but has hardly been addressed. Ideally, surface modification should offer excellent blood-environment compatibility, such as high dispersity in the blood environment, self-anticoagulant ability, and prevention of exogenously stimulated thrombosis, and enable some essential functions such as loading drugs. Here, we show that biointerface engineering empowers swarming magnetic nanorobots to operate powerfully and safely in blood environments. Specifically, while the high magnetic response from inner MB cores bestows the strong thrust in high-ionic-strength biological media under an alternating magnetic field $\mathbf{B}(t)$, the surface heparinoid-PSS brushes can endow the HPB-NRs with a high surface charge density. Moreover, different from the ion screening of surface charges on naked colloidal particles (*68*), the HPB-NRs show increasing charge density with the increasing ion concentration due to the compression of surface PSS brushes. Thus, the HPB-NRs have a high affinity to AT III and show strong short-range electrostatic repulsions with one another and with the constituents in blood environments (e.g., RBCs and VECs). In this way, they demonstrate good self-anticoagulation, reversible agglomeration-free reconfigurations, low hemolysis, and strong anti-bioadhesion in blood environments, largely reducing the risks and side effects from themselves. In contrast, MNRs modified with liquid hydrophobic perfluorocarbon coating can be effectively propelled in dense biological media (e.g., whole blood and dense vitreous body) by minimizing viscous drag (*2*, *29*) but suffer from poor dispersity, random agglomeration, and immune clearance in real blood environments. The MNRs cloaked with cell membranes seem to operate safely in vivo but are still restrained by difficult preservation and easy deactivation (*30*, *69*).

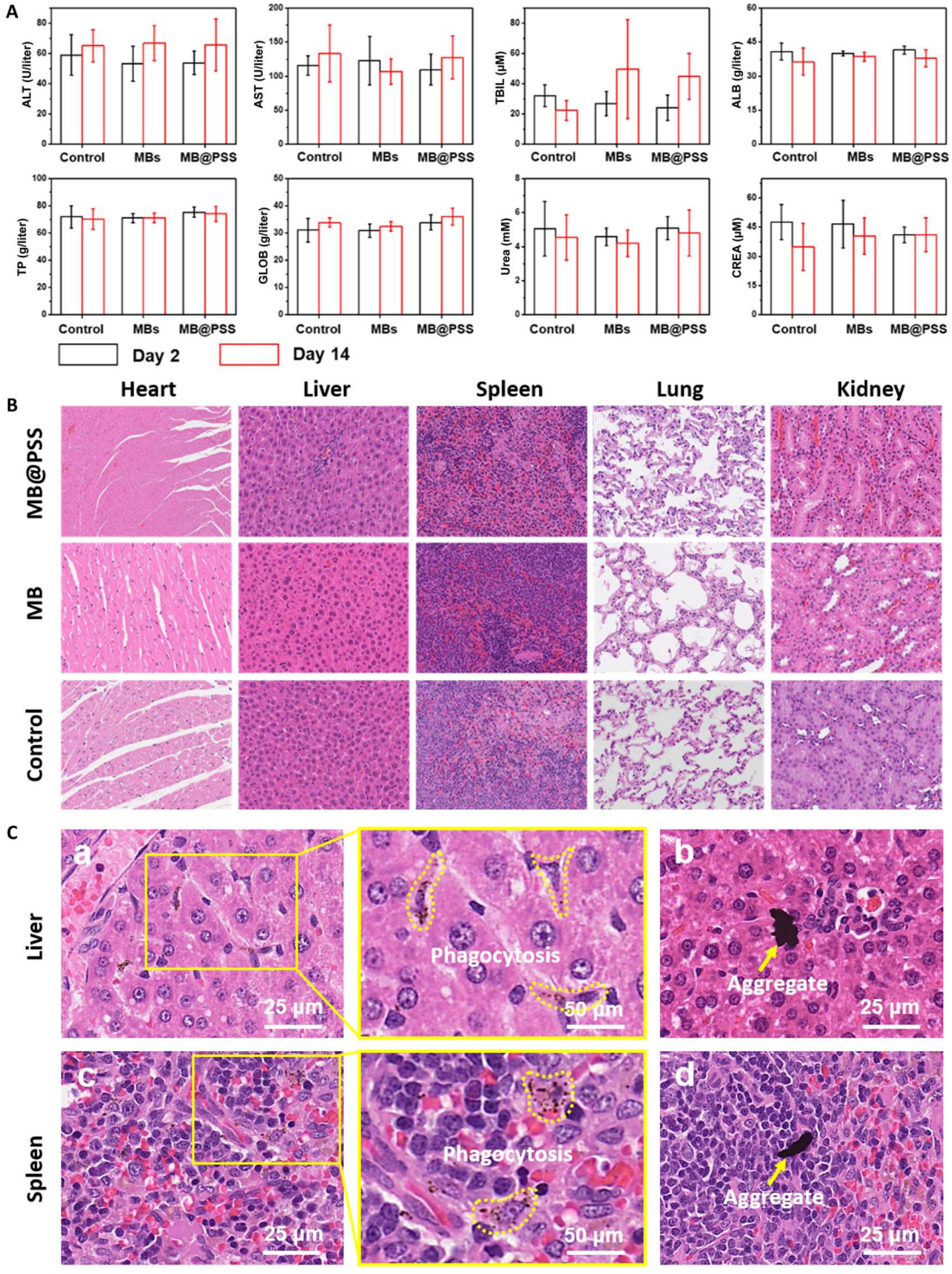

Fig. 7. In vivo safety analysis. (**A**) Blood biochemistry analysis. ALT, AST, TBIL, ALB, TP, and GLOB are common markers for hepatic toxicity. Urea and CREA are the markers for renal toxicity. (**B**) H&E-stained histological sections of major organs, including heart, liver, spleen, lung, and kidney, from the control group, mice treated with MBs and MB@PSS NPs for 14 days, respectively. (**C**) Biodistributions of the MB@PSS NPs (a and c) and MBs (b and d) in liver and spleen tissues at 14 days after injection.

The swarming HPB-NRs can rapidly deliver a large amount of thrombolytic drug to a thrombus and penetrate deeply into the thrombus to perform thrombolysis efficiently via synergistic effects of mechanical destruction and targeted drug delivery. Immobile drug nanocarriers and single MNRs generally suffer from long accumulation time at target thrombus sites and also cannot effectively penetrate into thrombi consisting of abundant platelet and well-organized fibrin (*33*, *70*, *71*). In our strategy, the swarming NRs are constructed by superparamagnetic NPs elaborately grafted with heparinoid-PSS brushes, with which they have rich drug binding sites on the surface and a high t-PA loading capacity of 123.6 mg g^{-1}. Thus, with powerful collective motions, they can deliver a large amount of thrombolytic drug within a short period of time to a thrombus and enhance the diffusion and penetration of the released t-PA. On the other hand, they can also generate mechanical forces to disrupt the cross-linked fibrin, facilitating their deep penetration and on-site drug release inside the thrombus. By taking advantage of the synergistic effects of mechanical destruction and targeted drug delivery, the swarming HPB-NRs can perform thrombolysis efficiently.

The main limitation of the swarming HPB-NRs for thrombolysis is that the building blocks still have a relatively large size (*13*), leading to difficulties in rapid biodegradation and complete excretion from the body after the thrombolytic task was accomplished. Thus, reducing the diameter of the building blocks of HPB-NRs is necessary to further enhance their biological safety. In addition, autonomous navigation of the swarming HPB-NRs may be required when facing thrombus in complex torturous small vessels (e.g., cerebral thrombus), and it is expected to be realized by developing computer programs to coordinate imaging apparatus, artificial intelligence navigation planners, and magnetic field generators (*72*).

In summary, we have developed an HPB biointerfacing strategy for swarming magnetic nanorobots that can perform safe and efficient thrombolysis in vivo. The experimental results show that the HPBs in the building blocks of nanorobots can endow the nanorobots with a high surface charge density, which can further increase with ion concentration in the medium. Thus, they show good self-anticoagulation, reversible agglomeration-free reconfigurations, low hemolysis (4.8%), and strong anti-bioadhesion in blood environments. This further makes them eliminate the risk of secondary thrombosis from themselves. The in vitro and in vivo experiments have confirmed that the swarming HPB-NRs can safely and efficiently perform thrombolysis by synergistic "motile-targeting" drug delivery and mechanical destruction, and a femoral vein thrombus in a rat model can be completely dissolved within 4 hours by the t-PA–loaded HPB-NRs. It is anticipated that the swarming HPB-NRs can also safely treat more challenging thrombotic disorders such as cerebral stroke and pulmonary embolism because of their excellent hemocompatibility and high thrombolytic efficacy. In addition, they may also act as a general motile platform to load and deliver different positively charged or positive charge–modified drugs for targeted therapies, such as targeted tumor therapy and infection control. This work provides a rational multifaceted HPB biointerfacing design strategy for biomedical nanorobots and may largely promote the development of motile MNR-based therapeutics for thrombolysis.

MATERIALS AND METHODS

Preparation of MB@PSS NPs

MB@PSS NPs were synthesized by surface-initiated ATRP, as illustrated in fig. S1. The raw NPs of MBs with a superparamagnetic iron oxide core and a SiO_2 shell (MBs, MagneStar MS500-SiOH) were purchased from Suzhou Nanomicro Technology Co. Ltd. (Suzhou, China). They were at first washed with Piranha solution [H_2SO_4:H_2O_2 = 7:3 (v/v)] for 1 min to remove the organic residues on the surfaces. To obtain MBs with surface -NH_2 groups, the freshly washed MBs were placed in a vial containing 2 ml of (3-aminopropyl) triethoxysilane and kept at 110°C for 1 hour under N_2 atmosphere and then washed with tetrahydrofuran (THF) three times. After that, 200 μl of α-bromoisobutyryl bromide and 10 mg of 2,2-bipyridyl were added into 5 ml of the THF solution containing MBs (5 mg/ml) with surface -NH_2 groups, kept at room temperature for 24 hours, and then washed with deionized (DI) water and ethanol three times, respectively, to get intermediate MBs. Last, the MB@PSS NPs were obtained after performing ATRP polymerization over the intermediate MBs. In detail, 400 mg of sodium styrene sulfonate, 10 mg of 2, 2-bipyridyl, and 5 mg of CuBr were dissolved in a 1:1 mixture of THF and water (3 ml) to give a reaction solution, into which the intermediate MBs were added. Subsequently, the system was degassed for three pump cycles and then at 80°C for 6 hours under an N_2 atmosphere. After the reaction was quenched by exposure to the air, the obtained MB@PSS NPs were separated from the solution immediately by magnetic separation and washed with DI water thoroughly. The MB@PSS NPs with different PSS brush lengths were obtained at different polymerization time (*t*). MB@PSS-2, MB@PSS-4, MB@PSS-6, MB@PSS-8, and MB@PSS-10 represent those MB@PSS NPs obtained at *t* of 2, 4, 6, 8, and 10 hours, respectively.

Characterizations of MB@PSS NPs

Morphologies of the samples were characterized by an S-4800 field-emission scanning electron microscope (Hitachi Ltd., Tokyo, Japan) at an acceleration voltage of 10.0 kV. The FTIR spectra of the samples were obtained on a Nicolet-60SXB FTIR spectrometer (Thermo Nicolet Co., Madison, WI, USA). The scanning range is from 400 to 4000 cm^{-1}, and the resolution is 4 cm^{-1}. ζ and hydrodynamic size of the MB@PSS NPs were determined by using the 90Plus Particle Size Analyser (Brookhaven Instruments Corporation, NY, USA), and the measurements were carried out at 25°C. The average ζ was calculated after nine times of repeated measurements, and the analysis was performed using the Smoluchowski model. The hydrodynamic size of the MB@PSS NPs was obtained by calculating the average of three times (five measurements each time) at an angle of 90°.

Magnetic propulsions of HPB-NRs

The magnetic actuation experiments were conducted in a customized three-axis Helmholtz electromagnetic coil setup fixed on an inverted optical microscope (Leica DM3000B, Germany). At first, a 55-μl DMEM suspension of the MB@PSS NPs (0.1 mg/ml) was added into a glass-bottom tank and placed in the working space of the electromagnetic coils. Then, an alternating magnetic field $\mathbf{B}(t)$ [e.g., a precessing or rotating $\mathbf{B}(t)$] was applied by the electromagnetic coils that were controlled by a signal generator (NI USB-6343, USA) and voltage amplifiers (Aigtek ATA-309, Xi'an,

China). The magnetic propulsion of the HPB-NRs [i.e., crawling or rotating motion of MB@PSS NPs assembled under a precessing or rotating $\mathbf{B}(t)$] was observed and recorded through the optical microscope. The speed of HPB-NRs was analyzed using the Video Spot Tracker V08.01 software, and more than six HPB-NRs were analyzed to obtain statistical results.

Hemolytic assay

Hemolytic assays of the samples were conducted using freshly obtained heparin sodium–stabilized rabbit blood samples. First, 2 ml of blood sample was added to 5 ml of phosphate-buffered saline (PBS), and then RBCs were isolated from serum by centrifugation at 1500 rpm for 10 min. The RBCs were further washed three times with PBS solution. The purified blood was diluted to 10 ml of PBS. Here, RBC incubation with DI water and PBS were used as the positive and negative controls, respectively. Then, 0.5 ml of diluted RBC suspension was added to 2 ml of unmodified MBs, MB@PSS NPs without [$-\mathbf{B}(t)$] and with [$+\mathbf{B}(t)$] the presence of the applied $\mathbf{B}(t)$ (B_0 = 10 mT, f = 5 Hz). All the sample tubes were kept under static condition at 37°C for 3 hours. Last, the mixtures were centrifuged at 1500 rpm for 5 min, and 100 μl of supernatant of all samples was transferred to a 96-well plate. The absorbance values of the supernatants at 540 nm were determined by using a Multiskan Go plate reader (Thermo Fisher Scientific, USA). The percent hemolysis of MB@PSS was calculated using the following formula:

$$Hemolysis\ (\%) = (OD_{\text{sample}} - OD_{\text{negative control}})/(OD_{\text{postive control}} - OD_{\text{negative control}}) * 100\%$$

Anticoagulation evaluation

APTT, PT, TT, and FIB were tested to evaluate the anticoagulation activity of the samples in vitro. The detection methods are as follows: 1.8 ml of freshly obtained blood was added into 0.2 ml of MB@PSS NP suspension (5 mg/ml). Then, centrifugal separation of 1 ml of plasma from mixed blood was prewarmed at 37°C for 3 min, and 50 μl of APTT, PT, TT, and FIB reagents was added to the 50-μl mixed solution, respectively. Four coagulation indicators (APTT, PT, TT, and FIB) were determined using an automatic blood coagulation analyzer (Sysmex CS-5100, Japan). All tests were repeated three times and averaged as results. To test whole blood coagulation activity, 100 μl of freshly obtained rabbit blood (without anticoagulant) was mixed with 100 μl of MBs, MB@PSS-2, MB@PSS-4, MB@PSS-6, MB@PSS-8, and MB@PSS-10 suspensions (1 mg/ml), and incubated at 37°C for 10 min. Then, 2 ml of DI water was added to the blood sample and centrifuged at 1500 rpm for 5 min. One hundred microliters of supernatant of all samples was transferred to a 96-well plate. The absorbance values of the supernatants at 540 nm were determined by using a Multiskan Go plate reader.

Cell culture and viability assay

VECs were purchased from the Shanghai Cell Bank of the Chinese Academy of Sciences. The cell culture media were prepared by using DMEM with 1% penicillin/streptomycin mixture from Capricorn and 10% fetal bovine serum from Life Technologies. All cells were incubated in an incubator at 37°C with 5% CO_2. Cell viability assay: 50,000 cells ml^{-1} (100 μl per well) were seeded in a 96-well plate. After cell seeding for 12 hours, DMEM in each well was replaced with fresh DMEM containing different concentrations of MB@PSS NPs (100 μl per well). For control, cells were not exposed to the MB@PSS NPs by adding PBS buffer. After incubation for 24 hours, removing the medium, each well was added to complete DMEM containing 10% CCK-8 and further incubated for another 2 hours. Last, absorbance intensities of the solution in the 96-well plate were measured at a wavelength of 450 nm by a Multiskan Go plate reader to determine cell viability.

Loading and fibrinolytic activity of t-PA

To load t-PA on the MB@PSS NPs, t-PA was at first coated with PL by incubating 100 μl of t-PA (1 mg/ml) with 500 μl of PL (100 mg/ml) for 10 min. Then, the obtained t-PA@PL NPs were incubated with 500 μl of MB@PSS NPs (1 mg/ml) for 20 min to obtain the t-PA–loaded building blocks after magnetic separation. The content of the loaded t-PA was quantified by the BCA protein assay kit (Macklin, Shanghai, China). The activity of the t-PA was tested using a chromogenic substrate (S-2288) (Macklin, Shanghai, China), as previously reported (*73*). The t-PA–loaded MB@PSS NPs were added to the Multiskan Go plate reader containing assay buffer [0.1 M^{-1} of tris-HCl (pH 7.4)] and S-2288 (1.0 mM^{-1}) at 37°C. The activity was calculated by absorbance at 405 nm at a different time of reaction.

In vitro thrombolysis

To form a thrombus, fresh rabbit blood was drawn into a 5-ml syringe (without anticoagulant) and kept under static condition until complete coagulation. To test thrombolysis of the swarming HPB-NRs in a glass artificial vasculature, a piece of thrombus was placed in a microwell connected with microchannels, and the t-PA–loaded HPB-NRs were actuated and navigated to move toward the thrombus through the microchannel under $\mathbf{B}(t)$ with B_0 of 10 mT and f of 5 Hz. The dissolution of the thrombus was recorded by continuously observing the shape change of the thrombus under an optical microscope (Leica DM3000B, Germany). To quantitively evaluate the thrombolysis, 200 μl of PBS suspension of the t-PA–loaded MB@PSS NPs (1 mg/ml) was added to 2 ml of PBS buffer containing a large piece of thrombus (150 ± 5 mg) and then actuated by $\mathbf{B}(t)$ with B_0 of 10 mT and f of 5 Hz for 6 hours [NRs + t-PA + $\mathbf{B}(t)$ group]. Then, the released fibrin and hemoglobin from the thrombus were determined by measuring the optical density at 410 nm (OD_{410}) and 540 nm (OD_{540}) of the supernatant. After the measurement, the liquid was removed from the tube, and the blood clot was weighed to obtain the weight loss. The percentage of weight loss was calculated to assess the thrombolysis rate. As a comparison, the fibrin and hemoglobin release and thrombolysis rate were also tested by exposing the thrombus to PBS buffer (control), moving HPB-NRs [NRs + $\mathbf{B}(t)$], t-PA, immobile t-PA–loaded MB@PSS (NRs + t-PA), and moving t-PA–loaded HPB-NRs [NRs + t-PA + $\mathbf{B}(t)$ group] using the same procedure, respectively.

In vivo thrombus model establishment

The SD rats weighing 200 ± 10 g were purchased from Wuhan Hualianke Biotechnology Co. Ltd. (Wuhan, China). All experiments on rats followed the *Guide for the Care and Use of Laboratory Animals* published by the Ministry of Health of the People's Republic of China. The SD rats were fed ad libitum and kept in a constant temperature and humidity environment on a 12-hour light/dark cycle. After an adjustment period of 3 days, the animals were divided into five groups.

To establish an SD rat femoral vein thrombus model, an SD rat was anesthetized through intraperitoneal injection (10% chloral hydrate) and immobilized supinely. A vertical slit (5 cm) was made in the middle of its inguen along the inner side of its thigh to reveal the femoral vein. Then, a piece of filter paper (3 × 5 mm, soaked with 20 wt % $FeCl_3$) was wrapped around the femoral vein. After 90 s, the femoral vein was washed with excessive saline. The venous thrombus would form within 5 min when the femoral vein became partially black and its far end slightly swelled.

In vivo thrombolysis

To investigate thrombolysis by swarming HPB-NRs, the building blocks of t-PA–loaded MB@PSS NPs (100 μl, 1 mg/ml) were at first injected into the bloodstream distal to the femoral vein thrombus of an SD rat and then collected at the upstream of the thrombus site with a blood flow velocity near zero using an N52 magnet (R = 2.5 mm, L = 5 mm) for 10 min. Then, a rotating $\mathbf{B}(t)$ with B_0 of 10 mT and f of 5 Hz was applied to actuate the swarming t-PA–loaded HPB-NRs to achieve thrombolysis. The t-PA–loaded HPB-NRs were tracked in real time using a P8-VET ultrasound imaging system (Dawei, China), of which the central frequency, power output, and contrast gain were set to be 14 MHz, 10%, and 46 dB, respectively. The laser speckle blood flow monitoring system (LSBFMS) was used to monitor the blood flow before and after the thrombus model was prepared. The blood flow in the femoral vein was monitored, recorded, and analyzed using a moorFLPI-2 LSBFMS (Moor Instruments, London, UK). The statistical software (SPSS 24.0) was used to analyze the collected blood flow data and evaluate the thrombolytic efficacy. The thrombolytic efficacy of other groups, such as the control, NRs + $\mathbf{B}(t)$, t-PA, NRs + t-PA, and NRs + t-PA + $\mathbf{B}(t)$ group, was also investigated.

Safety evaluation of MB@PSS in vivo

SD rats (weighing 200 ± 10 g) were selected as the mice into which 100 μl of the solution was injected via the tail vein. After acclimatization to the environment, the rats were separated into six groups [normal saline (control group), suspensions of MBs, and MB@PSS (1 mg/ml) for toxicity tests at 2 and 14 days, respectively (n = 4 for each group)]. Then, the mice were euthanized at 2 and 14 days, and blood samples and the main organs were collected for blood biochemical panel and histological analysis.

Supplementary Materials

This PDF file includes:
Supplementary Text
Figs. S1 to S17
Legends for movies S1 to S14

Other Supplementary Material for this manuscript includes the following:
Movies S1 to S14

REFERENCES AND NOTES

1. D. Jin, K. Yuan, X. Du, Q. Wang, S. Wang, L. Zhang, Domino reaction encoded heterogeneous colloidal microswarm with on-demand morphological adaptability. *Adv. Mater.* **33**, e2100070 (2021).
2. J. Yu, D. Jin, K.-F. Chan, Q. Wang, K. Yuan, L. Zhang, Active generation and magnetic actuation of microrobotic swarms in bio-fluids. *Nat. Commun.* **10**, 5631 (2019).
3. B. Yigit, Y. Alapan, M. Sitti, Programmable collective behavior in dynamically self-assembled mobile microrobotic swarms. *Adv. Sci.* **6**, 1801837 (2019).
4. Q. Wang, L. Zhang, External power-driven microrobotic swarm: From fundamental understanding to imaging-guided delivery. *ACS Nano* **15**, 149–174 (2021).
5. J. Yu, B. Wang, X. Du, Q. Wang, L. Zhang, Ultra-extensible ribbon-like magnetic microswarm. *Nat. Commun.* **9**, 3260 (2018).
6. H. Chen, H. Zhang, T. Xu, J. Yu, An overview of micronanoswarms for biomedical applications. *ACS Nano* **15**, 15625–15644 (2021).
7. M. Su, Q. Dai, C. Chen, Y. Zeng, C. Chu, G. Liu, Nano-medicine for thrombosis: A precise diagnosis and treatment strategy. *Nanomicro Lett.* **12**, 96 (2020).
8. J. Shao, M. Abdelghani, G. Shen, S. Cao, D. S. Williams, J. C. M. van Hest, Erythrocyte membrane modified janus polymeric motors for thrombus therapy. *ACS Nano* **12**, 4877–4885 (2018).
9. Q. Deng, L. Zhang, W. Lv, X. Liu, J. Ren, X. Qu, Biological mediator-propelled nanosweeper for nonpharmaceutical thrombus therapy. *ACS Nano* **15**, 6604–6613 (2021).
10. H. Zhou, C. C. Mayorga-Martinez, S. Pane, L. Zhang, M. Pumera, Magnetically driven micro and nanorobots. *Chem. Rev.* **121**, 4999–5041 (2021).
11. R. Dreyfus, J. Baudry, M. L. Roper, M. Fermigier, H. A. Stone, J. Bibette, Microscopic artificial swimmers. *Nature* **437**, 862–865 (2005).
12. M. Yang, X. Guo, F. Mou, J. Guan, Lighting up micro-/nanorobots with fluorescence. *Chem. Rev.* **123**, 3944–3975 (2023).
13. L. Wang, X. Hao, Z. Gao, Z. Yang, Y. Long, M. Luo, J. Guan, Artificial nanomotors: Fabrication, locomotion characterization, motion manipulation, and biomedical applications. *Interdiscip. Mater.* **1**, 256–280 (2022).
14. J. Ou, K. Liu, J. Jiang, D. A. Wilson, L. Liu, F. Wang, S. Wang, Y. Tu, F. Peng, Micro-/nanomotors toward biomedical applications: The recent progress in biocompatibility. *Small* **16**, e1906184 (2020).
15. Z. Wu, Y. Chen, D. Mukasa, O. S. Pak, W. Gao, Medical micro/nanorobots in complex media. *Chem. Soc. Rev.* **49**, 8088–8112 (2020).
16. J. Wang, Y. Dong, P. Ma, Y. Wang, F. Zhang, B. Cai, P. Chen, B.-F. Liu, Intelligent micro/nanorobot for cancer theragnostic. *Adv. Mater.* **34**, e2201051 (2022).
17. Z. Cong, S. Tang, L. Xie, M. Yang, Y. Li, D. Lu, J. Li, Q. Yang, Q. Chen, Z. Zhang, X. Zhang, S. Wu, Magnetic-powered janus cell robots loaded with oncolytic adenovirus for active and targeted virotherapy of bladder cancer. *Adv. Mater.* **34**, e2201042 (2022).
18. F. Mou, C. Chen, H. Ma, Y. Yin, Q. Wu, J. Guan, Self-propelled micromotors driven by the magnesium–water reaction and their hemolytic properties. *Angew. Chem. Int. Ed.* **52**, 7208–7212 (2013).
19. B. E. de Avila, P. Angsantikul, J. Li, M. Angel Lopez-Ramirez, D. E. Ramirez-Herrera, S. Thamphiwatana, C. Chen, J. Delezuk, R. Samakapiruk, V. Ramez, M. Obonyo, L. Zhang, J. Wang, Micromotor-enabled active drug delivery for in vivo treatment of stomach infection. *Nat. Commun.* **8**, 272 (2017).
20. X. Wei, M. Beltran-Gastelum, E. Karshalev, B. Esteban-Fernandez de Avila, J. Zhou, D. Ran, P. Angsantikul, R. H. Fang, J. Wang, L. Zhang, Biomimetic micromotor enables active delivery of antigens for oral vaccination. *Nano Lett.* **19**, 1914–1921 (2019).
21. Z. Yang, L. Wang, Z. Gao, X. Hao, M. Luo, Z. Yu, J. Guan, Ultrasmall enzyme-powered janus nanomotor working in blood circulation system. *ACS Nano* **17**, 6023–6035 (2023).
22. A. C. Hortelao, C. Simó, M. Guix, S. Guallar-Garrido, E. Julián, D. Vilela, L. Rejc, P. Ramos-Cabrer, U. Cossío, V. Gómez-Vallejo, T. Patiño, J. Llop, S. Sánchez, Swarming behavior and in vivo monitoring of enzymatic nanomotors within the bladder. *Sci. Robot.* **6**, eabd2823 (2021).
23. F. Zhang, Z. Li, Y. Duan, A. Abbas, R. Mundaca-Uribe, L. Yin, H. Luan, W. Gao, R. H. Fang, L. Zhang, J. Wang, Gastrointestinal tract drug delivery using algae motors embedded in a degradable capsule. *Sci. Robot.* **7**, eabo4160 (2022).
24. F. Zhang, J. Zhuang, Z. Li, H. Gong, B. E.-F. de Ávila, Y. Duan, Q. Zhang, J. Zhou, L. Yin, E. Karshalev, W. Gao, V. Nizet, R. H. Fang, L. Zhang, J. Wang, Nanoparticle-modified microrobots for in vivo antibiotic delivery to treat acute bacterial pneumonia. *Nat. Mater.* **21**, 1324–1332 (2022).
25. B. Wang, K. F. Chan, K. Yuan, Q. Wang, X. Xia, L. Yang, H. Ko, Y.-X. J. Wang, J. J. Y. Sung, P. W. Y. Chiu, L. Zhang, Endoscopy-assisted magnetic navigation of biohybrid soft microrobots with rapid endoluminal delivery and imaging. *Sci. Robot.* **6**, eabd2813 (2021).
26. H. Zhang, Z. Li, C. Gao, X. Fan, Y. Pang, T. Li, Z. Wu, H. Xie, Q. He, Dual-responsive biohybrid neutrobots for active target delivery. *Sci. Robot.* **6**, eaaz9519 (2021).
27. B. Esteban-Fernández de Ávila, W. Gao, E. Karshalev, L. Zhang, J. Wang, Cell-like micromotors. *Acc. Chem. Res.* **51**, 1901–1910 (2018).
28. X. Zhan, J. Wang, Z. Xiong, X. Zhang, Y. Zhou, J. Zheng, J. Chen, S.-P. Feng, J. Tang, Enhanced ion tolerance of electrokinetic locomotion in polyelectrolyte-coated microswimmer. *Nat. Commun.* **10**, 3921 (2019).

29. Z. Wu, J. Troll, H.-H. Jeong, Q. Wei, M. Stang, F. Ziemssen, Z. Wang, M. Dong, S. Schnichels, T. Qiu, P. Fischer, A swarm of slippery micropropellers penetrates the vitreous body of the eye. *Sci. Adv.* **4**, eaat4388 (2018).
30. C. Gao, Y. Wang, Z. Ye, Z. Lin, X. Ma, Q. He, Biomedical micro-/nanomotors: From overcoming biological barriers to in vivo imaging. *Adv. Mater.* **33**, e2000512 (2021).
31. J. Hu, S. Huang, L. Zhu, W. Huang, Y. Zhao, K. Jin, Q. ZhuGe, Tissue plasminogen activator-porous magnetic microrods for targeted thrombolytic therapy after ischemic stroke. *ACS Appl. Mater. Interfaces* **10**, 32988–32997 (2018).
32. M. Xie, W. Zhang, C. Fan, C. Wu, Q. Feng, J. Wu, Y. Li, R. Gao, Z. Li, Q. Wang, Y. Cheng, B. He, Bioinspired soft microrobots with precise magneto-collective control for microvascular thrombolysis. *Adv. Mater.* **32**, e2000366 (2020).
33. M. Wan, Q. Wang, R. Wang, R. Wu, T. Li, D. Fang, Y. Huang, Y. Yu, L. Fang, X. Wang, Y. Zhang, Z. Miao, B. Zhao, F. Wang, C. Mao, Q. Jiang, X. Xu, D. Shi, Platelet-derived porous nanomotor for thrombus therapy. *Sci. Adv.* **6**, eaaz9014 (2020).
34. J. Zheng, R. Qi, C. Dai, G. Li, M. Sang, Enzyme catalysis biomotor engineering of neutrophils for nanodrug delivery and cell-based thrombolytic therapy. *ACS Nano* **16**, 2330–2344 (2022).
35. L. Wang, J. Wang, J. Hao, Z. Dong, J. Wu, G. Shen, T. Ying, L. Feng, X. Cai, Z. Liu, Y. Zheng, Guiding drug through interrupted bloodstream for potentiated thrombolysis by C-shaped magnetic actuation system in vivo. *Adv. Mater.* **33**, e2105351 (2021).
36. R. Cheng, W. Huang, L. Huang, B. Yang, L. Mao, K. Jin, Q. ZhuGe, Y. Zhao, Acceleration of tissue plasminogen activator-mediated thrombolysis by magnetically powered nanomotors. *ACS Nano* **8**, 7746–7754 (2014).
37. Q. Wang, X. Du, D. Jin, L. Zhang, Real-time ultrasound doppler tracking and autonomous navigation of a miniature helical robot for accelerating thrombolysis in dynamic blood flow. *ACS Nano* **16**, 604–616 (2022).
38. Q. Wang, D. Jin, B. Wang, N. Xia, H. Ko, B. Y. M. Ip, T. W. H. Leung, S. C. H. Yu, L. Zhang, Reconfigurable magnetic microswarm for accelerating tPA-mediated thrombolysis under ultrasound imaging. *IEEE ASME Trans. Mechatron.* **27**, 2267–2277 (2022).
39. X. Tang, L. Manamanchaiyaporn, Q. Zhou, C. Huang, L. Li, Z. Li, L. Wang, J. Wang, L. Ren, T. Xu, X. Yan, Y. Zheng, Synergistic integration and pharmacomechanical function of enzyme-magnetite nanoparticle swarms for low-dose fast thrombolysis. *Small* **18**, e2202848 (2022).
40. M. A. Macchione, C. Biglione, M. Strumia, Design, synthesis and architectures of hybrid nanomaterials for therapy and diagnosis applications. *Polymers* **10**, 527 (2018).
41. H. Arami, A. Khandhar, D. Liggitt, K. M. Krishnan, In vivo delivery, pharmacokinetics, biodistribution and toxicity of iron oxide nanoparticles. *Chem. Soc. Rev.* **44**, 8576–8607 (2015).
42. L. H. Reddy, J. L. Arias, J. Nicolas, P. Couvreur, Magnetic nanoparticles: Design and characterization, toxicity and biocompatibility, pharmaceutical and biomedical applications. *Chem. Rev.* **112**, 5818–5878 (2012).
43. T. Yin, Y. Li, Y. Ren, A. R. M. Fuad, F. Hu, R. Du, Y. Wang, G. Wang, Y. Wang, Phagocytosis of polymeric nanoparticles aided activation of macrophages to increase atherosclerotic plaques in Apoe$^{-/-}$ mice. *J. Nanobiotechnol.* **19**, 121 (2021).
44. S. J. Paluck, T. H. Nguyen, H. D. Maynard, Heparin-mimicking polymers: Synthesis and biological applications. *Biomacromolecules* **17**, 3417–3440 (2016).
45. X. Liu, L. Yuan, D. Li, Z. Tang, Y. Wang, G. Chen, H. Chen, J. L. Brash, Blood compatible materials: State of the art. *J. Mater. Chem. B* **2**, 5718–5738 (2014).
46. K. Matyjaszewski, Advanced materials by atom transfer radical polymerization. *Adv. Mater.* **30**, e1706441 (2018).
47. X. Guo, M. Ballauff, Spherical polyelectrolyte brushes: Comparison between annealed and quenched brushes. *Phys. Rev. E Stat. Nonlin. Soft Matter Phys.* **64**, 051406 (2001).
48. J. Ge, Y. Hu, T. Zhang, T. Huynh, Y. Yin, Self-assembly and field-responsive optical diffractions of superparamagnetic colloids. *Langmuir* **24**, 3671–3680 (2008).
49. J. M. Peula, A. Fernández-Barbero, R. Hidalgo-Álvarez, F. J. de las Nieves, Comparative study on the colloidal stability mechanisms of sulfonate latexes. *Langmuir* **13**, 3938–3943 (1997).
50. L. O. Mair, B. A. Evans, A. Nacev, P. Y. Stepanov, R. Hilaman, S. Chowdhury, S. Jafari, W. Wang, B. Shapiro, I. N. Weinberg, Magnetic microkayaks: Propulsion of microrods precessing near a surface by kilohertz frequency, rotating magnetic fields. *Nanoscale* **9**, 3375–3381 (2017).
51. D. Ahmed, T. Baasch, N. Blondel, N. Laubli, J. Dual, B. J. Nelson, Neutrophil-inspired propulsion in a combined acoustic and magnetic field. *Nat. Commun.* **8**, 770 (2017).
52. C.-H. Ooi, Y. P. Ling, W. Z. Abdullah, A. Z. Mustafa, S.-Y. Pung, F.-Y. Yeoh, Physicochemical evaluation and in vitro hemocompatibility study on nanoporous hydroxyapatite. *J. Mater. Sci. Mater. Med.* **30**, 44 (2019).
53. M. Xin, L. Ren, Y. Sun, H.-h. Li, H.-S. Guan, X.-X. He, C.-X. Li, Anticoagulant and antithrombotic activities of low-molecular-weight propylene glycol alginate sodium sulfate (PSS). *Eur. J. Med. Chem.* **114**, 33–40 (2016).
54. J. Klein, Hydration lubrication. *Friction* **1**, 1–23 (2013).
55. J. Yu, N. E. Jackson, X. Xu, Y. Morgenstern, Y. Kaufman, M. Ruths, J. J. de Pablo, M. Tirrell, Multivalent counterions diminish the lubricity of polyelectrolyte brushes. *Science* **360**, 1434–1438 (2018).
56. D. Lu, Y. Jin, X. Wang, L. Xie, Q. Liu, Y. Chen, H. Wang, Z. Lei, Heparin-like anticoagulant polypeptides with tunable activity: Synthesis, characterization, anticoagulative properties and clot solubilities in vitro. *Mater. Sci. Eng. C Mater. Biol. Appl.* **129**, 112405 (2021).
57. A. S. Drozdov, A. Y. Prilepskii, E. M. Koltsova, E. I. Anastasova, V. V. Vinogradov, Magnetic polyelectrolyte-based composites with dual anticoagulant and thrombolytic properties: Towards optimal composition. *J. Sol-Gel Sci. Technol.* **95**, 771–782 (2020).
58. L. Zhang, C. Chen, J. Zhang, B. Liu, G. Teng, J. Wang, X. Zhang, D. Cai, Z. Wu, Alternating magnetic field-responsive nanoplatforms for controlled imidacloprid release and sustainable pest control. *ACS Sustain. Chem. Eng.* **9**, 10491–10502 (2021).
59. S. Wang, X. Guo, W. Xiu, Y. Liu, L. Ren, H. Xiao, F. Yang, Y. Gao, C. Xu, L. Wang, Accelerating thrombolysis using a precision and clot-penetrating drug delivery strategy by nanoparticle-shelled microbubbles. *Sci. Adv.* **6**, eaaz8204 (2020).
60. S. Z. Goldhaber, H. Bounameaux, Pulmonary embolism and deep vein thrombosis. *Lancet* **379**, 1835–1846 (2012).
61. J. A. Heit, Epidemiology of venous thromboembolism. *Nat. Rev. Cardiol.* **12**, 464–474 (2015).
62. M. Di Nisio, N. van Es, H. R. Bueller, Deep vein thrombosis and pulmonary embolism. *Lancet* **388**, 3060–3073 (2016).
63. J. Xu, J. Zhou, Y. Zhong, Y. Zhang, J. Liu, Y. Chen, L. Deng, D. Sheng, Z. Wang, H. Ran, D. Guo, Phase transition nanoparticles as multimodality contrast agents for the detection of thrombi and for targeting thrombolysis: In vitro and in vivo experiments. *ACS Appl. Mater. Interfaces* **9**, 42525–42535 (2017).
64. Y. Zhong, Y. Zhang, J. Xu, J. Zhou, J. Liu, M. Ye, L. Zhang, B. Qiao, Z.-G. Wang, H.-T. Ran, D. Guo, Low-intensity focused ultrasound-responsive phase-transitional nanoparticles for thrombolysis without vascular damage: A synergistic nonpharmaceutical strategy. *ACS Nano* **13**, 3387–3403 (2019).
65. J. Xu, Y. Zhang, J. Xu, G. Liu, C. Di, X. Zhao, X. Li, Y. Li, N. Pang, C. Yang, Y. Li, B. Li, Z. Lu, M. Wang, K. Dai, R. Yan, S. Li, G. Nie, Engineered nanoplatelets for targeted delivery of plasminogen activators to reverse thrombus in multiple mouse thrombosis models. *Adv. Mater.* **32**, e1905145 (2020).
66. A. K. Gupta, M. Gupta, Synthesis and surface engineering of iron oxide nanoparticles for biomedical applications. *Biomaterials* **26**, 3995–4021 (2005).
67. C. D. Walkey, J. B. Olsen, H. Guo, A. Emili, W. C. Chan, Nanoparticle size and surface chemistry determine serum protein adsorption and macrophage uptake. *J. Am. Chem. Soc.* **134**, 2139–2147 (2012).
68. M. A. Brown, A. Goel, Z. Abbas, Effect of electrolyte concentration on the stern layer thickness at a charged interface. *Angew. Chem. Int. Ed.* **55**, 3790–3794 (2016).
69. M. Xuan, J. Shao, J. Li, Cell membrane-covered nanoparticles as biomaterials. *Natl. Sci. Rev.* **6**, 551–561 (2019).
70. W. Cao, Y. Liu, P. Ran, J. He, S. Xie, J. Weng, X. Li, Ultrasound-propelled janus rod-shaped micromotors for site-specific sonodynamic thrombolysis. *ACS Appl. Mater. Interfaces* **13**, 58411–58421 (2021).
71. S. Hassanpour, H.-J. Kim, A. Saadati, P. Tebon, C. Xue, F. W. van den Dolder, J. Thakor, B. Baradaran, J. Mosafer, A. Baghbanzadeh, N. R. de Barros, M. Hashemzaei, K. J. Lee, J. Lee, S. Zhang, W. Sun, H.-J. Cho, S. Ahadian, N. Ashammakhi, M. R. Dokmeci, A. Mokhtarzadeh, A. Khademhosseini, Thrombolytic agents: Nanocarriers in controlled release. *Small* **16**, e2001647 (2020).
72. T. Li, X. Chang, Z. Wu, J. Li, G. Shao, X. Deng, J. Qiu, B. Guo, G. Zhang, Q. He, L. Li, J. Wang, Autonomous collision-free navigation of microvehicles in complex and dynamically changing environments. *ACS Nano* **11**, 9268–9275 (2017).
73. J. N. Marsh, G. Hu, M. J. Scott, H. Zhang, M. J. Goette, P. J. Gaffney, S. D. Caruthers, S. A. Wickline, D. Abendschein, G. M. Lanza, A fibrin-specific thrombolytic nanomedicine approach to acute ischemic stroke. *Nanomedicine* **6**, 605–615 (2011).

Acknowledgments

Funding: This work was supported by the National Natural Science Foundation of China (nos. 52073222 and 21474078), the National Key Research and Development Project (no. 2021YFA1201400), the Innovation Team in Key Areas of the Innovation Talent Promotion Plan (2021) of MOST of China, the Natural Science Foundation of Hubei Province (no. 2019CFA048), and the Open Foundation of the State Key Laboratory of Advanced Technology for Materials Synthesis and Processing (Wuhan University of Technology, 2023-KF-5). **Author contributions:** F.M. and J.G. proposed the concept. M.Y., F.M., and Z.L. designed the experiments. M.Y., C.C., and L.Y. carried out the synthesis, structural characterization, and propulsion tests. M.Y., Y.Z., and Z.L. carried out animal experiments. M.Y., Y.Z., F.M., C.C., Z.L., and J.G. cowrote the manuscript. J.G. supervised the project. All authors discussed the results and participated in analyzing the experimental results. **Competing interests:** The authors declare that they have no competing interests. **Data and materials availability:** All data needed to evaluate the conclusions in the

paper are present in the paper and/or the Supplementary Materials. Source data are available in the Supplementary Materials.

Submitted 7 September 2023
Accepted 30 October 2023
Published 29 November 2023
10.1126/sciadv.adk7251